AN ABSTRACT OF THE THESIS OF

Xinyuan Chong for the degree of Doctor of Philosophy in Electrical and Computer Engineering presented on June 9, 2017.

Title: Surface-Enhanced Infrared Absorption Gas Sensing Incorporating Advanced Plasmonic Nanostructures and Nano-Composite Materials.

Abstract approved:

_____

Alan X. Wang

This dissertation focuses on extending the application scope of surface enhanced infrared absorption spectroscopy to gas sensing. The method we propose is incorporating plasmonic nanostructures with nano-composite material, metal-organic framework, which can selectively preconcentrate certain gas molecules into the nanopores. The preconcentrating property is first demonstrated by applying metal-organic framework to optical fiber based sensor. Then two different metal-organic framework integrated surface enhanced infrared absorption gas sensors fabricated on bulk substrate and nano-membrane are investigated, and the high enhancement factors demonstrated for the first time. Lastly, an on-chip spectrometer using high resolution plasmonic filter array is proposed and experimentally demonstrated for resolving CO_2 absorption spectrum at 2.0 μm with 10 ~ 12 nm resolution. This filter array spectrometer is simple and low-cost, which can be potentially used for portable gas spectroscopy system.

Surface-Enhanced Infrared Absorption Gas Sensing Incorporating Advanced Plasmonic Nanostructures and Nano-Composite Materials

by
Xinyuan Chong

A THESIS

submitted to

Oregon State University

in partial fulfillment of
the requirements for the
degree of

Doctor of Philosophy

Presented June 9, 2017
Commencement June 2017

Doctor of Philosophy thesis of Xinyuan Chong presented on June 9, 2017

APPROVED:

Major Professor, representing Electrical and Computer Engineering

Director of the School of Electrical Engineering and Computer Science

Dean of the Graduate School

I understand that my thesis will become part of the permanent collection of Oregon State University libraries. My signature below authorizes release of my thesis to any reader upon request.

Xinyuan Chong, Author

ACKNOWLEDGEMENTS

I would like to express my appreciation to my advisor Professor Alan X. Wang for the guidance and advising through my graduate education. It was only because of his keen interest and careful supervision that gave my work this extent form. My appreciation also extends to Professor Chih-Hung Chang, Professor Larry Cheng, Professor Matthew Johnston and Professor William H. Warnes for serving as my committee members.

I also would like to thank all my current and former laboratory colleagues (Erwen Li, Qian Gao, Xianming Kong, Shiwen Li, Kenny Squire, Spencer Liverman, Fanghui Ren, Jing Yang, and Yuting Xi) and collaborators (Dr. Paul Ohodnicki, Dr. Ki-Joong Kim, and Yujing Zhang) for their academic support and friendship.

I want to specially acknowledge with gratitude, the support and love of my family. The completion of my Ph.D. study would not have been possible without them.

Finally, I want to thank for the financial support from National Science Foundation under Grant No. 1449383, National Energy Technology Laboratory (NETL) under the RES contract DE-FE0004000 and graduate fellowship from NETL.

TABLE OF CONTENTS

Page

TABLE OF CONTENTS (Continued)

Page

LIST OF FIGURES

Figure Page

LIST OF FIGURES (Continued)

Figure Page

LIST OF FIGURES (Continued)

Figure Page

LIST OF FIGURES (Continued)

Figure Page

LIST OF TABLES

Table Page

CHAPTER 1. INTRODUCTION

Gas sensing has a great impact across a wide range of application in both industry and academia: Petrochemical and automotive industry[1], where sensors are used to ensure the safety, monitor process and control the pollution; Medical application[2-4], where exhaled gases are analyzed for diagnosis; Indoor air quality supervision[5-7], where some of the toxic gases are detected, such as carbon monoxide; Atmospheric science[8-10], where the profile and pathways of different gas species are monitored for environmental studies. In the past several decades, various of technologies have been established, such as laboratory analytical equipment gas chromatographs[11, 12], ultra-low-cost pellistors[13], metal oxide semiconductor (MOS) sensors[14-16], electrochemical sensors[17-19], acoustic sensors [20-22] and optical sensors[23-25]. However, each technology has its strengths and weaknesses. Table 1.1 summarizes the advantages, disadvantages and the application fields for different gas sensing technologies.

Table 1.1 Summary of common gas sensing technologies[26]

Technologies	Advantages	Disadvantages	Target Gases and Application Field
Gas Chromatograph	(a) Excellent separation performance (b) High sensitivity and selectivity	(a) High cost (b) Difficulty in miniaturization	Typical laboratory analysis

Pellistors	(a) Robust; (b) Harsh environment	Zero drift at ppm level	Flammable gases in combustion
Metal Oxide Semiconductor	(a) Low cost (b) Short response time (c) Wide range of target gases (d) Long lifetime	(a) Relatively low sensitivity and selectivity (b) Sensitive to environmental factors (c) High energy consumption	Industrial applications and civil use
Electrochemical Sensors	(a) High sensitive (b) High specificity	Short lifetime	Industrial applications and civil use
Acoustic Sensors	(a) Long lifetime (b) Avoiding secondary pollution	(a) Low sensitivity (b) Sensitive to environmental change	Components of Wireless Sensor Networks
Optical Sensors	(a) High sensitivity, selectivity and stability (b) Long lifetime (c) Insensitive to environment change	(a) Difficulty in miniaturization (b) High cost	(a) Remote air quality monitoring (b) Gas leak detection systems with high accuracy and safety (c) High-end market applications

As listed in Table 1.1, in contrast to the other technologies, gas sensors based on optics can achieve high specificity, minimal drift, fast response and much longer

lifetime. Moreover, the measurement can be conducted in real time and in-situ without disturbing the system (e.g. combustion system).

In this chapter, optical gas sensing techniques will be reviewed. Among them, surface plasmon resonance (SPR) based techniques will be discussed in details, especially, the reported applications and challenges of surface enhanced infrared absorption (SEIRA) spectroscopy. Then a new nano-porous material, metal-organic framework (MOF) will be introduced as well as its application in sensing techniques.

1.1. Optical Gas Sensing Techniques

Common optical gas sensing techniques can be categorized into two groups: absorption based techniques and non-absorption based techniques. Absorption based techniques are more common, non-absorption based techniques are usually used for special applications.

Absorption based techniques are conceptually simple, which is based on Beer-Lambert law[27]:

$$I = I_0 exp(-\alpha L) \tag{1.1}$$

where I is the intensity of the light to have passed through the sensor or gas sample, I_0 is the intensity of the incident light, α is the absorption coefficient of the gas (a function of the gas concentration and wavelength) and L is the optical path-length. Most of the gases of interest have characteristic infrared absorption bands between 2 μm and 20 μm, such as CO, CO_2, CH_4, NO, N_2O, NO_2, NH_3, HCN, HF, SO_2,

SF_6, H_2S, volatile organic compound and water vapor. Absorption based techniques include Non-dispersive infrared (NDIR)[28], UV absorption[29], Fourier transform infrared (FTIR) spectroscopy[30], tunable diode laser spectroscopy (TDLS)[31], Photoacoustic spectroscopy (PAS)[32] and Cavity ring-down spectroscopy (CRDS)[33].

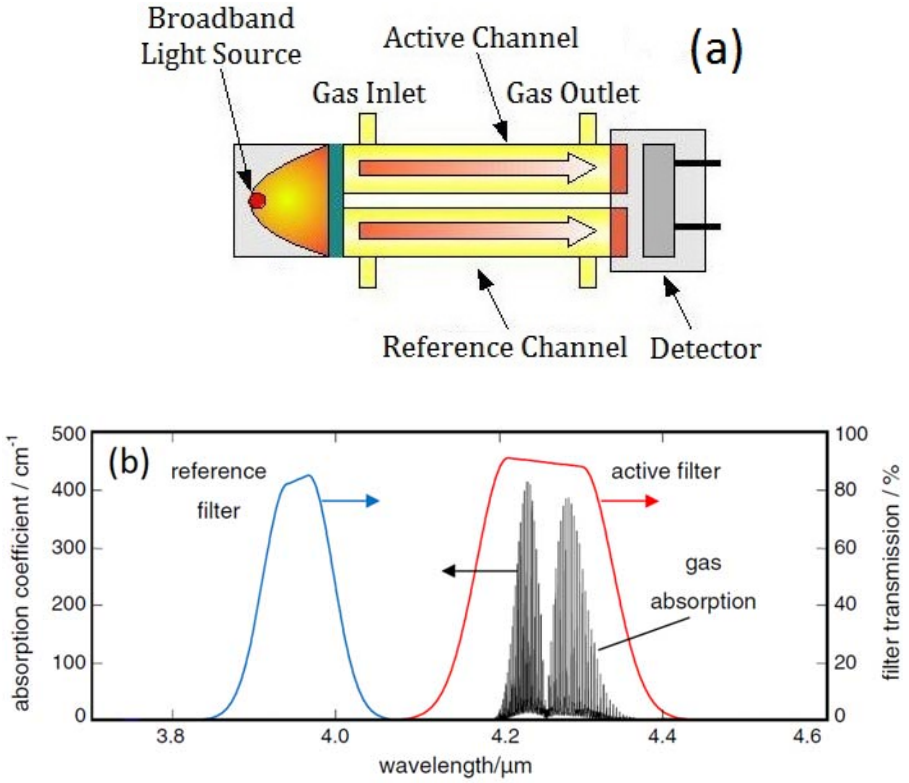

Figure. 1.1. (a) Illustration of NDIR measurement setup. (b) The absorption spectrum of CO_2 is superimposed on the transmission spectra of active and reference channel filters[34].

The NDIR technique is one of the simplest gas sensing techniques. Typically, it contains a broadband light source, a gas cell, two filters and detectors. Light from the broadband source first passes through two filters, one covering the whole absorption band of the gas sample (active channel) and the other covering a neighboring non-absorbing region (reference channel). Both filters must be carefully selected to ensure that no other gas species' absorption band within their transmitted windows. Figure 1.1 shows a typical filter characteristics for CO_2 sensing, as an example. Then the transmitted lights of both channels are collected by the detectors. The reference channel is used to compensate the fluctuation of the light source, which is assumed to affect both channels in equal proportion. Although the configuration of the NDIR sensor is very simple, several issues limit its application, especially in near-infrared (NIR, 0.8 μm ~ 2.5 μm) region: (1) Broadband light sources are usually highly divergent. Therefore, the detection limit over a long path length will depend on the emission power of the light source at the absorption band region. (2) At NIR region, the absorption bands of some gases (e.g. CO_2 and CO) are not well separated. Filters need to be selected very carefully to avoid the cross-response. (3) The absorption bands at NIR region are typically the overtones or combinations of the fundamental vibration bands in mid-infrared (MIR), which are much weaker and require longer path length to obtain desired detection limit[34].

Figure 1.2. The photograph of a Brewer spectrophotometer[35].

UV absorption is mainly used for O_3 detection, which has strong absorption at 254 nm. Stratospheric O_3 plays a very important role in protecting life from harmful UV. Mercury lamps as the source are used widely in ambient AQ monitoring, which can determine O_3 with sub-ppb level. O_3 is also monitored in process stream in water treatment, food processing and other industries. Figure 1.2 shows an example of the detection systems that use solar radiation as the source to monitor O_3 in the upper atmosphere, which is called as Brewer spectrophotometer[35].

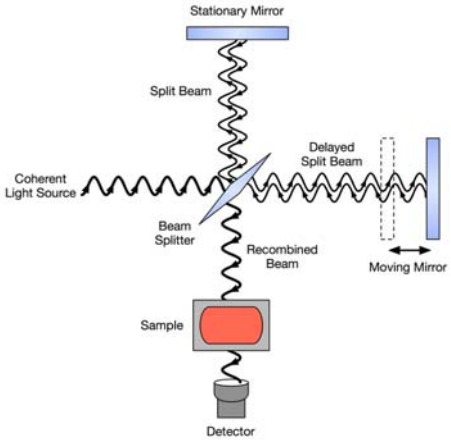

Figure 1.3 Schematic of FTIR interferometer[36].

FTIR spectrometer is the most commonly used commercial infrared absorption spectroscopy system. Typically, it is based on the Michelson interferometer[37] as shown in Figure 1.3. The interferometer consists of a beam splitter, a fixed mirror, and a mirror that translates back and forth, very precisely. The beam splitter is made of a special material that transmits half of the radiation striking it and reflects the other half. Radiation from the source strikes the beam splitter and separates into two beams. One beam is transmitted through the beam splitter to the fixed mirror and the second is reflected off the beam splitter to the moving mirror. The fixed and moving mirrors reflect the radiation back to the beam splitter. Again, half of this reflected radiation is transmitted and half is reflected at the beam splitter, resulting in one beam passing to the detector and the second back to the source. Finally, a Fourier transform analysis on the interferogram will be performed to obtain the spectrum.

Compared to a scanning spectrometer (monochromator), there are three advantages for an FT spectrometer[38]: First, the multiplex advantage. This arises from the fact that information from all wavelengths is collected simultaneously, which results in a higher signal-to-noise ratio for a given scan time. In practice multiple scans are often averaged, increasing the signal-to-noise ratio by the square root of the number of scans. Second, the throughput advantage. This results from the fact that in a dispersive instrument, the entrance and exit slits restrict the amount of light passing through it, while the interferometer throughput is only determined by the diameter of the collimated beam coming from the source. Lastly, the wavelength accuracy advantage. The wavelength scale is calibrated by a laser beam of known wavelength that passes through the interferometer. This is much more stable and accurate than in dispersive instruments where the scale depends on the mechanical movement of diffraction gratings. In practice, the accuracy is limited by the divergence of the beam in the interferometer, which depends on the resolution.

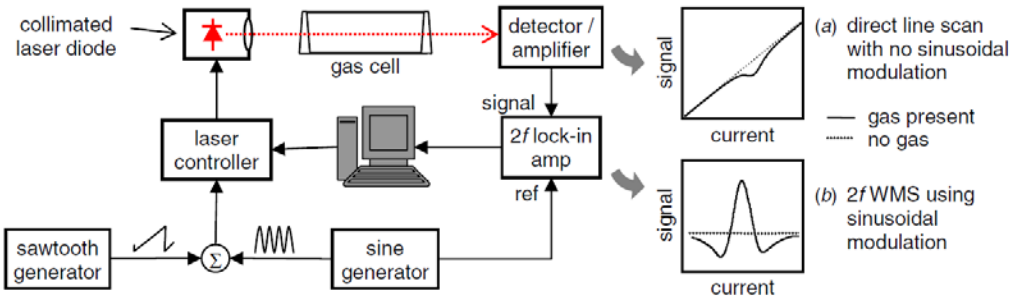

Figure. 1.4. Conventional configuration of TDLS: (a) direct line scan and (b) 2nd harmonic wavelength modulation spectroscopy[34].

In order to achieve very high spectral resolution, tunable diode lasers are used instead of the broadband light source in spectroscopic system, which is called TDLS. As shown in Figure 1.4, in TDLS, light from a laser is transmitted through a sample containing the target gas and by tuning the wavelength to one of the gas's absorption lines and measuring the absorption, the concentration of the gas can be determined. By accurately controlling the laser temperature and the drive current, the wavelength may be tuned precisely to a specific absorption line that can be selected to be free of interfering absorption from other compounds, thus conferring high specificity[35]. Working at such high resolution provides TDLS several advantages: high signal to noise ratio resulting from fully resolved absorption lines and narrow effective baselines, high specificity to the gas samples and fast operation speed with up to MHz modulation frequency.

The major issue that limits the detection sensitivity of TDLS is the optical interference fringes caused by mirrors, lenses, optical fiber end, detector and laser head windows. Since the gas absorption line is very narrow, to resolve the individual lines, the use of lasers with narrower emission line are required. However, the narrow laser emission linewidth will result in a long coherence length, which means these interference effects are unavoidable for such high-resolution spectroscopy[34].

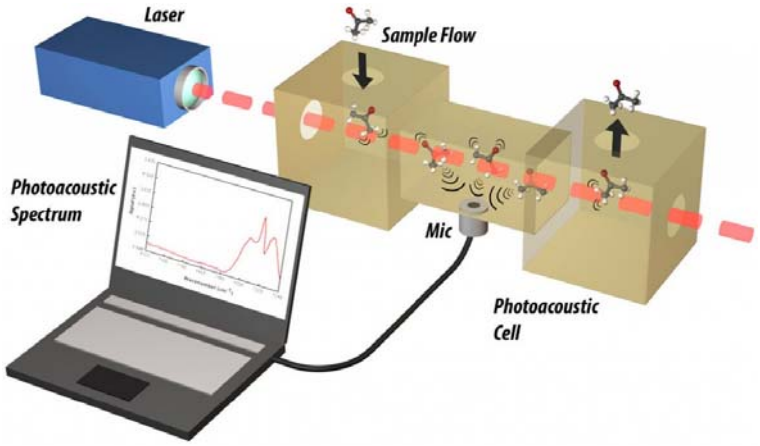

Figure 1.5. Schematic photoacoustic spectroscopy system[39].

PAS and CRDS are more specialized techniques. PAS relies on the fact that gases will expand when they absorb IR radiation, as shown in Figure 1.5. If the gas is pulsed at audio frequencies by an IR source when enclosed in a sealed container, pressure pulses are created which can be detected by a high-sensitivity microphone. By enclosing the gas sample in a cylindrical chamber/cell, the sound signal is amplified by tuning the modulation frequency to an acoustic resonance of the cell. PAS is highly stable and sensitive and can achieve sub-ppb limits of detection for some gases. A disadvantage of photoacoustic systems is that they are highly sensitive to background acoustic noise and vibrations. In field use, this can be the performance-limiting feature, yet it can vary from site to site and is hard to predict[34].

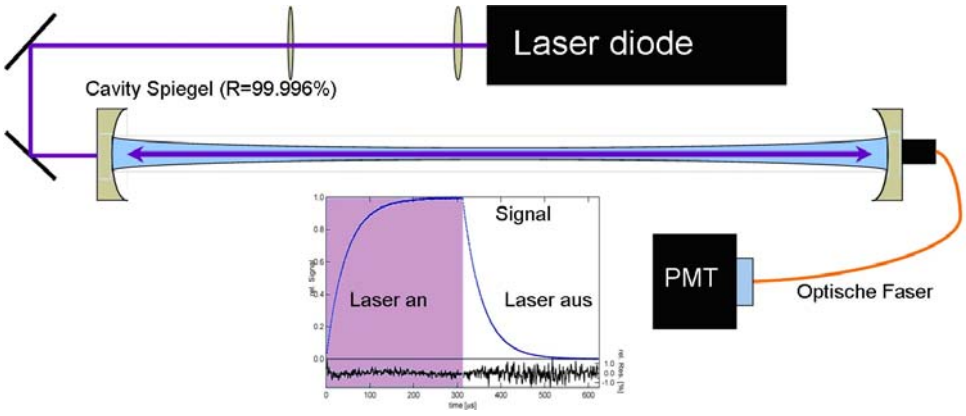

Figure 1.6. Schematic drawing of the cavity ring-down instrument[40].

CRDS system (Figure 1.6) uses a laser to illuminate a high-finesse optical cavity, which consists of a sample cell with two highly reflective mirrors on both ends. The laser is turned off to allow the measurement of the exponentially decaying light intensity leaking from the cavity. During this decay, light is reflected back and forth many thousands of times between the mirrors, yielding an effective path-length in the order of a few kilometers. When a gas that absorbs the light is inside the cavity, the light intensity decreases faster than without gas, and the CRDS system measures the time taken for the light to decay to 1/e of its initial intensity, the "ringdown time", which is used to determine the gas concentration. Because of the very large effective path-length, it is exceptionally sensitive and can determine some compounds at ppt levels.

In contrast, non-absorption techniques are less common and usually used in special applications. There are three commonly used non-absorption techniques: gas chemiluminescence (CL), UV fluorescence and Raman spectroscopy. CL is a

process whereby a gas reacts with another compound to emit light. The intensity of emission is related to the concentration of target gas. CL is mostly used in low concentrations of NO_x detection, particularly in the ambient air quality control. The NO in air reacts with O_3 and is oxidized to produce NO_2 and O_2. And as excited NO_2 molecules return to the ground state, they emit light with a peak at around 1200 nm, which is usually detected by a photomultiplier tube. UV fluorescence also mainly used in air quality control for low level SO_2 detection. When irradiated by UV light, the SO_2 gas molecules absorb the light between 190 and 230 nm, creating excited SO_2 molecules. When the excited SO_2 molecules decay to a lower energy state, fluorescence light at longer wavelengths (230 ~ 420 nm) will be emitted, whose intensity is proportional to the SO_2 concentration[35]. Raman shift is also a "fingerprint" of molecules which can be used to detect and identify gases. Raman spectroscopy is especially useful for detection of hydrogen gas, because the hydrogen molecule does not have absorption bands from the near ultraviolet to near infrared that can be used for optical absorption based detection[41].

Recent years, the trend has been moved away from large stand-alone analytical systems (chromatographs and IR spectrometers, etc.). The need for miniature devices has rapid grown. These miniaturized devices are portable, low-power, low- weight, low-cost and integratable with other devices. Thank for the development in nanotechnology, a great deal of research has been directed toward the miniaturization of gas sensors. Recently, new sensing concept, surface plasmon

resonance, appeared which offers good promises for the design of robust miniature sensors[42].

1.2. Plasmonic Based Gas Sensing

1.2.1. Surface Plasmon Resonance

Surface plasmon resonance (SPR) refers to the collective oscillations of the conduction electrons in metallic nanostructures[43]. The intensity and the position of resonance strongly depend on the physical parameters and material properties of the nanostructures, as well as the dielectric properties of the surrounding environment. Due to this variety of responsive variables, in the past decade, SPR has developed various applications. SPR occurs in two distinct cases: propagating surface plasmon polaritons (SPPs) and localized SPR (LSPR) as shown in Figure 1.7. SPPs are the propagating charge oscillations on the surface of thin metal films. SPPs cannot be excited by free-space radiation. It requires momentum matching, such as through periodicity in a nanostructure, for resonance excitation. In contrast, LSPR occurs when the dimensions of a metallic nanostructure are less than the wavelength of incident light, leading to collective but non-propagating oscillations of surface electrons in the metallic nanostructure[44].

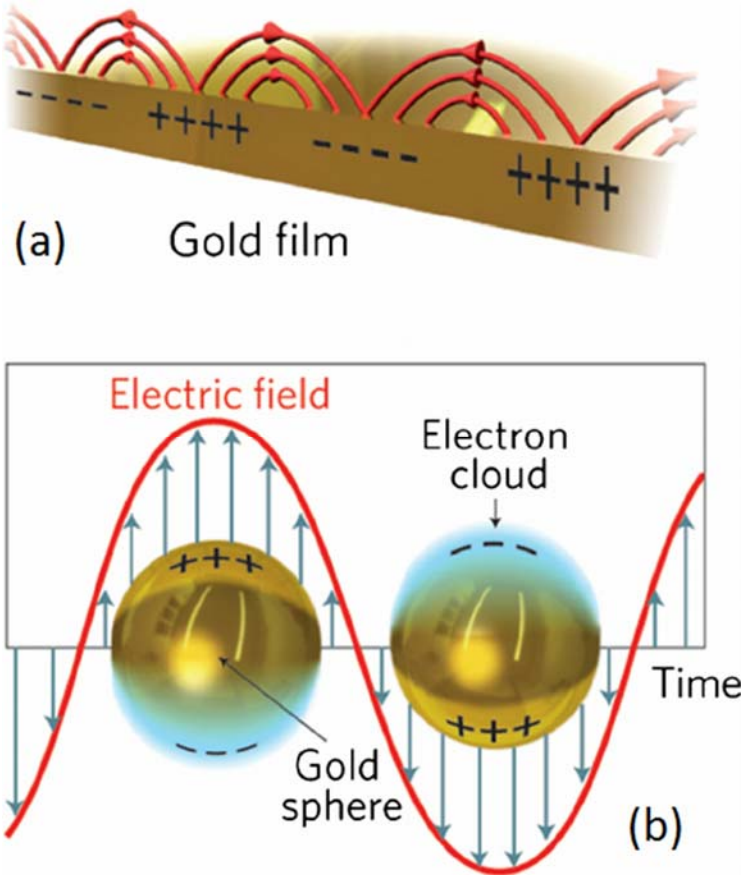

Figure 1.7 (a) Surface plasmon polaritons at metal and dielectric interface; (b) localized surface plasmon resonance at the metal nanoparticle surface[45].

Both SPPs and LSPR strongly depend on the refractive index of the surrounding medium, and can also concentrates the incident electromagnetic (EM) field around the nanostructure. The local EM field can influence optical processes such as fluorescence, Raman scattering and infrared absorption. By utilizing LSPR and/or SPP, numerous plasmonic metallic nanostructures have already been developed for sensitive optical sensing, such as plasmon-enhanced fluorescence

(PEF)[46-52], surface-enhanced Raman scattering (SERS)[53-55] and surface-enhanced infrared absorption (SEIRA) spectroscopy.

SPPs and/or LSPR based sensing techniques can be divided into two categories: transducer or signal amplifier. For functioning as a transducer, the main application is refractive index sensing, since the resonance position (wavelength or angle) is sensitive to the refractive index of the surrounding medium. Other signals, such as chemical reaction, biological binding or physical adsorption can be transduced to the change of resonance position. For the signal amplification, the main application is spectroscopy. As mentioned before, the EM field will be concentrated around the nanostructure, which will enhance the light-matter interaction, resulting in an enhanced spectroscopic signal. For example, Raman scattering is proportional to the forth order of the electric field, and infrared absorption is proportional to the square of the electric field.

1.2.2. Plasmonic Gas Sensing

When the plasmonic effect are adapted for gas sensing application, two sensing schemes emerge[56]: direct sensing and indirect sensing. In indirect sensing schemes, the plasmonic structure is located adjacent to some reagent-sensitive material and simply probes the dielectric changes in that system. In direct sensing configurations, the gas samples actively influence the plasmonic entity, changing its material properties and in turn its optical response. Several representative applications of both schemes will be introduced in the following paragraphs.

Most of the indirect sensing approaches rely on the gas-induced refractive index changes in the vicinity of plasmonic structures. Since the adsorption of gas molecules or the generation of new product during the chemical reaction causes large refractive index changes. For example, Bingham et al.[57] utilized high-resolution localized surface plasmon resonance spectroscopy on arrays of silver nanoparticles to detect gas-induced refractive index changes in the 10^{-4} range. When the gas sample was switched from He to the target gas, a spectral shift was observed in the extinction spectrum. The shift was determined by the weight and concentration of the target gas. Buso et al.[58] have utilized a SiO_2 matrix containing Au and NiO nanoparticles for sensitive detection of hydrogen, where the SiO_2 matrix was chosen due to its extremely high specific surface area. They found a plasmon resonance peak at 563 nm, which underwent a drastic blue shift of 22 nm when exposing it to 1 vol.% H_2 in dry air. Liu et al.[59] have reported an approach by putting a single palladium nanoparticle at the nanofocus of a gold nanoantenna. The strong near-field of the gold nanoantenna will sense the small refractive index change when H_2 molecules were adsorbed by palladium nanoparticle. Tang et al. investigated Au/Pd core-shell particles with different shapes, faceting, and Pd shell thickness for hydrogen sensing. A pronounced spectral redshift on the order of 25 nm was observed by using Au/Pd core-shell triangular plate.

In order to further improve the performance of plasmonic sensors, recent designs have moved towards complex or hybrid nanostructures, which can provide a way to improve the two main limiting factors for the sensitivity: the linewidth (quality factor) of the plasmon resonance spectrum and the background close to the resonance. For example, Nau et al.[60] used Au nanowires on top of a gasochromic WO_3 waveguide.

The coupling between the broad plasmon peak and the narrow waveguide mode leads to a sharp extinction dip, which is ideally suited for sensing due to its low FWHM. Powell et al. have used sliver nanocubes on top of silver thin film with a dielectric space layer between them. The gap plasmon mode generated strong field which is extremely sensitive to the refractive index of the surrounding environment.

On the other hand, the direct sensing application are mainly focused on simple optical transmission, absorption or reflection measurement. For example, Ando et al.[61] have demonstrated a plasmonically functionalized Au-CuO nanocomposite film for CO sensing. The absorbance measurements at a temperature of 300°C showed a plasmonic absorbance peak around 800 nm, which increased upon exposure of the film to 1000 ppm and 1% CO in dry air. A similar approach was presented by Sirinakis et al.[62], who used gold nanoparticles embedded in an yttria-stabilized zirconia matrix. Ohodnicki et al.[63] have utilized an Au/TiO_2 nanocomposite film for hydrogen detection at 850°C. The nanocomposite was prepared through sol-gel deposition techniques. A pronounced reversible and reproducible transmittance change was observed when expose to 4 vol.% H_2 in N_2 and Air alternatively. Ma et al.[64, 65] used an array of triangular silver nanoparticles fabricated by nanosphere lithography for chloroform vapor detection. A clear plasmon resonance around 670 nm, which decreased in magnitude upon exposure to increasing concentrations of chloroform vapor. Maeda et al.[66] utilized an array of rectangular subwavelength holes in a palladium film, fabricated by electron beam lithography, for hydrogen detection. When it was exposed to a concentration of 2 vol.% hydrogen, a decrease of the transmittance was observed.

Another important application of direct sensing scheme is the amplification of Raman scattering signals from molecules adsorbed on roughened or nanostructured metal surfaces, which is also referred as SERS. Different material and morphology of the nanostructures have been developed for SERS spectroscopy, which can reach the enhancement factors in the 10^{10} range. For example, Li et al.[67] have utilized small silica-coated gold nanoparticles to perform shell-isolated nanoparticle-enhanced Raman spectroscopy for hydrogen detection. Rae et al.[68] have used a mixed Ag/Pd nanoparticles substrate for CO and N_2O sensing. The SERS enhancement factor achieved were 4×10^5 and 1×10^5, respectively. Similar to SERS spectroscopy, SERIA spectroscopy is another possible direction application scheme for gas sensing. However, due to the intrinsically low absorption coefficient of gas molecules, there are not many reported results. Only Nishijima at el.[69] have demonstrated a ~27 times increase using metal nano-hole array for SF_6 gas detection.

1.2.3. Surface Enhanced Infrared Absorption Spectroscopy

Infrared absorption spectroscopy probes the vibrational modes of various molecular bonds, which can provide structural information of chemical and biological compounds in a label-free manner[70, 71]. Infrared absorption is governed by Beer-Lambert law. Given specific molecules, it requires either a long absorption path or a high density of target molecules to achieve significant infrared absorption. However, for molecules with small infrared absorption cross sections or very thin samples such as monolayers, conventional infrared absorption cannot provide good sensitivity.

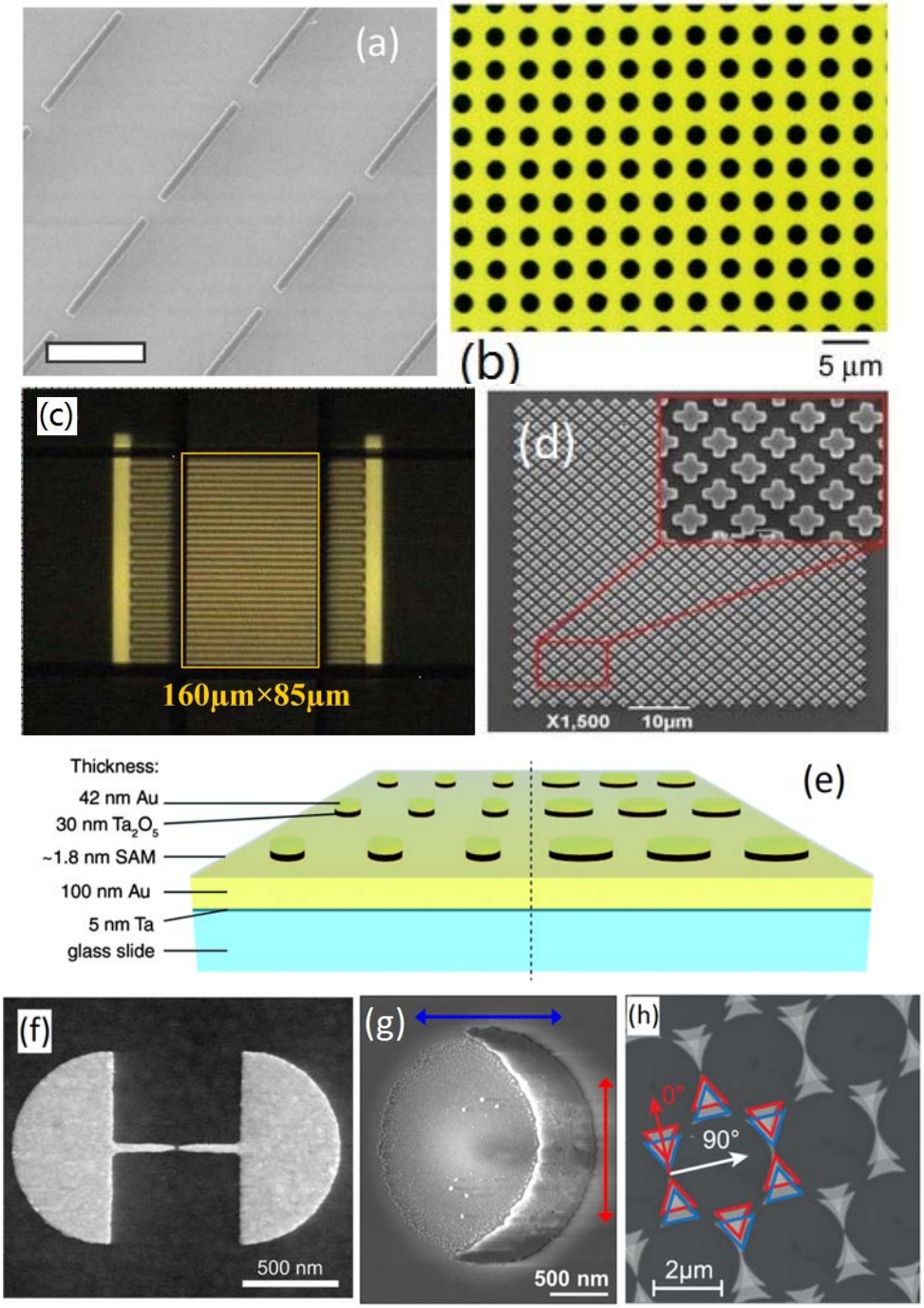

Figure 1.8. Different nanostructures applied to SERIA: (a) Nanowire array, (b) nano-hole array, (c) Au grating, (d) cross-shape absorber, (e) nano-disk array, (f) fan-shape antenna, (g) nano-crescent and (h) nano-triangle array[72-79].

To overcome this challenge, SEIRA spectroscopy, which leverages the strong light-matter interaction and subwavelength localization enabled by plasmonic resonances of metallic nanostructures, was first reported by Hartstein et al.[70] and Hatta et al.[80] in the 1980s. Initial studies in SEIRA focused on rough metal surface[81], metal island films[82] and metal nanoparticles (NPs)[83]. However, the extinction spectra were relatively broad and the plasmonic resonant wavelengths were difficult to control due to the random morphology and distribution of these metallic nanostructures. In recent years, rationally patterned metallic nanostructures with narrow extinction spectra and precisely determined resonant wavelengths due to the dipole-to-dipole interaction (such as nanowire[75], nanohole[77], strip grating[78], cross-shaped perfect absorber[79], nanodisk[72], fan-shaped nanoantennas[74], nanocrescents[76], and triangle-shaped nanoantennas[73] were applied to SEIRA) as shown in Figure 1.8. However, existing applications of SEIRA are exclusively focused on mid-infrared sensing of biomaterials or large chemical molecules, such as proteins or polymers.

SEIRA for gas detection, which is another Holy Grail application for infrared absorption spectroscopy, is yet not very successful due to several intrinsic drawbacks of SEIRA. First, the localized optical field of plasmonic nanostructures limits the light-matter interaction between gas molecules and the optical field. The enhanced infrared absorption can only come from the gas molecules located within the “hot-spots” of plasmonic nanostructures, which usually have very limited volume. Second, the absorption coefficients of gases are intrinsically lower than

solid or liquid materials due to the low molecular density. In order to extend the scope of SERIA to gas sensing, the solution we found is metal-organic framework (MOF).

1.3. Metal-Organic Framework for Optical Sensing Application

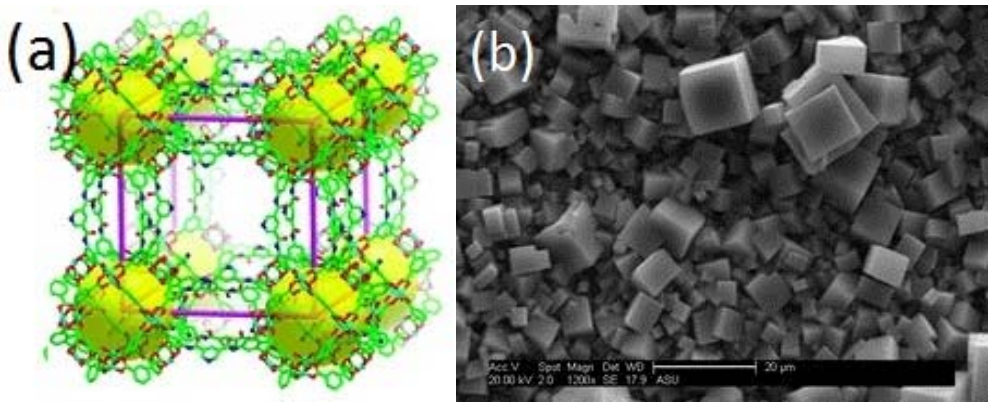

Figure 1.9. (a) Schematic of MOF; (b) The SEM image of MOF crystals[84, 85].

MOF is a new type of nanoporous crystalline materials consisting of metal ions and organic ligands as shown in Figure 1.9. MOFs possess many unique material properties such as high surface areas, tailorable chemistry and tunable nano-cavities, which make them very promising for different applications, such as gas storage[86-89], chemical separation[90-92], catalysis[93, 94], molecular recognition[95-97], drug delivery[98-100] and sensing[101-104]. Among all the applications, we are particularly interested in combining MOF with optical sensing techniques.

One of the application of MOF in optical sensing is SERS spectroscopy. Metallic colloids were widely employed as SERS substrates due primarily to ease of preparation and large SERS signal enhancement. A major challenge in using any surface enhanced spectroscopy for detection purposes is delivering the molecules of interest to the enhancing region, so-called hot spot. In SERS, the Raman signal of a molecule can be enhanced by many orders of magnitude, but close proximity (<3–5 nm) to a plasmonic surface or nanoparticle is key[105]. Most of the SERS application are focused on molecules that have strong affinity to plasmonic metal surfaces at ambient temperatures. However, many other molecules show low affinity toward the metal, thus limiting the use of SERS techniques in their detection. To address this issue, various techniques have been developed to capture molecules with low affinity for SERS detection. For example, a capture layer can be coated on the metal surface to bind the analytes. However, detection of non-adsorbing molecules in the vapor phase remains a challenge for SERS. One approach was developed by using MOF coated nanoparticles, which can adsorb the vapor phase analytes from the ambient environment and preconcentrate them. In addition, MOF can protect nanoparticles from aggregation[103, 106].

Another application of MOF is gas sensing based on refractive index change. Surface plasmon resonance has revolutionized optical sensing with its ability to measure extremely small changes in refractive index, which results in a variety of applications. The vast majority of work has focused on biological sensing, which can achieve the detection limits below 100 protein molecules. The low limits of

detection in these applications are possible due to the relatively large changes in RI associated with binding of bulky biomolecules. However, there are a limited number of reports of small molecule sensing, such as gas molecules, which is significantly more challenging due to small changes in RI. To solve this problem, MOF was integrated on the sensor surface to preconcentrate the gas molecules. With the help of MOF, a 14-fold signal enhancement was achieved[107].

1.4. Thesis Organization

Chapter 2 will show the characterization of the MOFs used in the work. The optical properties including refractive index and absorption are studied. The surface morphology of MOF thin films is also presented in this chapter.

In Chapter 3, in order to demonstrate capability of MOF being used in gas sensor, an ultra-short near-infrared fiber optic gas sensor using MOF was developed. The fabrication of the sensors and the experimental measurement results are presented in this chapter. Fiber-optic gas sensor with high sensitivity can be potentially applied for distributed sensing network.

Chapter 4 presents the development of plasmonic nano-structure fabricated on sapphire substrate hybrid with MOF for infrared absorption based gas sensing. This hybrid plasmonic-MOF device can effectively increase the infrared absorption path of on-chip gas sensors by adsorbing the gas molecules inside the MOF porous structures.

In Chapter 5, a suspended silicon nitride (Si_3N_4) nano-membrane device integrating plasmonic nano-patch antennas with MOF, which efficiently improved

the plasmonic enhancement comparing to the device presented in Chapter 4 by reducing the effective RI of the substrate. This device successfully extends the SEIRA to gas sensing for the first time, which proves a promising strategy for future on-chip gas sensing with ultra-compact size.

Chapter 6 presents an ultra-compact, cost-effective on-chip near-infrared spectroscopy system for CO_2 sensing using narrow-band optical filter array based on plasmonic gratings with a waveguide layer. The experimental results for resolving the vibrational bands of CO_2 at 2.0 μm wavelength proves the potential for future on-site IR spectroscopy system.

A brief summary and conclusion will be presented in Chapter 7.

CHAPTER 2. CHARACTERIZATION OF METAL-ORGANIC FRAMEWORK

In this chapter, we present the characterization of two different MOFs used in the experiment. The first MOF used is Cu-BTC (BTC=benzene-1,3,5-tricarboxylic acid), which is the most widely studied MOF material in thin-film form and has good adsorption capacity for CO_2. The other MOF used is zeolitic imidazolate framework-8 (ZIF-8), which has been extensively investigated due to its excellent thermal stability and selectivity toward CO_2. Besides, due to the hydrophobic surface property, water molecules can only be adsorbed at the outer surface, while CO_2 can diffuse into the inner pores.

2.1. Optical Property of Metal-Organic Framework

Since the application of MOFs in this work are optical sensing, obviously, the optical properties of MOF are very important for the design and device performance. Therefore, the optical properties are characterized at the very beginning. As shown in Figure 2.1(a), the refractive index of a roughly 200 nm Cu-BTC thin film are measured by an ellipsometry. The Cu-BTC thin film was grown on a Si wafer, which was used to obtain large RI difference between the sample and substrate, resulting in a more accurate result. Due to the high porosity nature of MOF, the RI of MOF is relative small, which is smaller than most of the commercially available substrates. From Figure 2.1(a), we can also find that the imaginary part of the RI is zero within the measured wavelength range. This is desired property for the

application, because there will be no absorption at this wavelength range to influence the absorption signals from CO_2 gas.

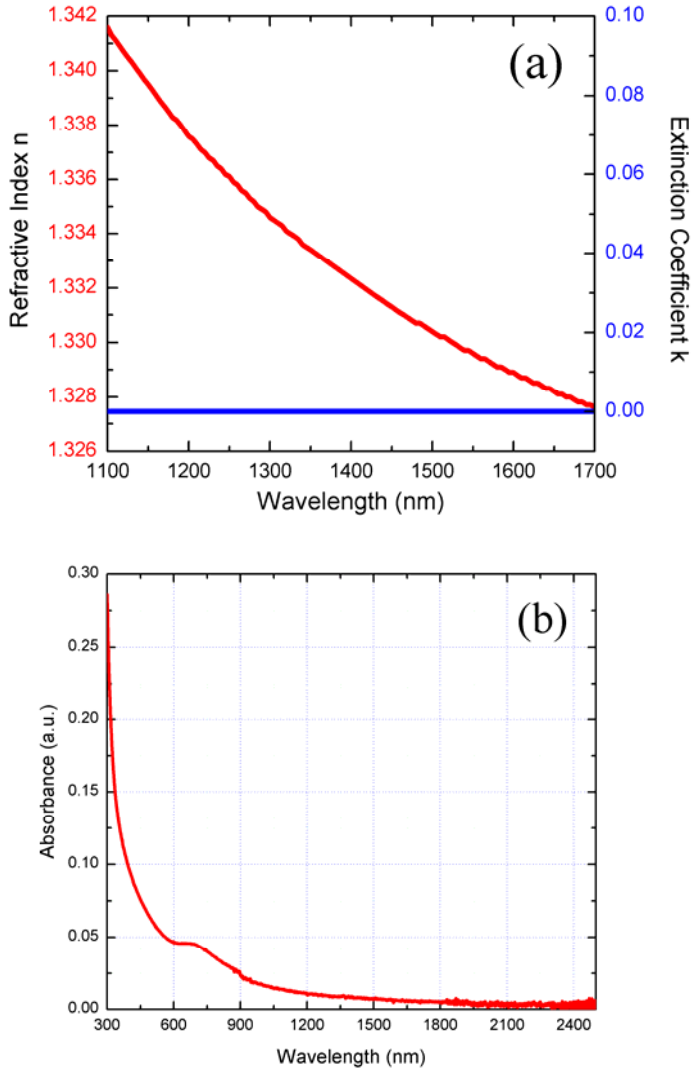

Figure 2.1. (a) The ellipsometry result of Cu-BTC thin film. (b) The absorption spectrum of 100 nm Cu-BTC thin film.

To further ensure this, the absorption spectrum of a 100 nm Cu-BTC thin film on sapphire substrate was measured by UV-vis-NIR spectrometer, as shown in Figure 2.1(b). Since the sapphire substrate is transparent at NIR region, if there is a absorption signal, it will be caused by the MOF. As shown in Figure 2.1(b), one absorption peak was observed around 700 nm, which is attributed to the d-d band absorption of typical copper carboxylate complexes in the crystal structure of Cu-BTC MOF. At CO_2 absorption band (1565–1585 nm), the absorption is very close to zero. Due to the approach that UV-Vis-NIR spectrometer measuring the absorbance, Figure 2.1(b) actually represents both absorption and scattering. Considering the highly rough surface of MOF layer, the small portion of "Absorbance" that is decreasing with wavelength is actually the scattering.

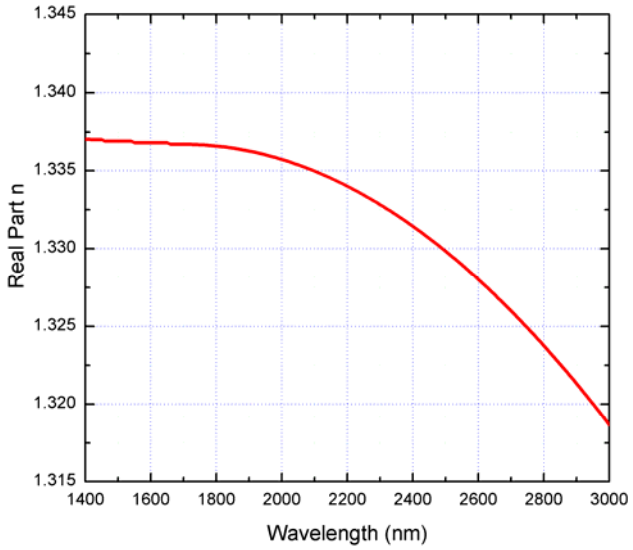

Figure 2.2 The ellipsometry result of ZIF-8 thin film.

Similarly, the RI of ZIF-8 thin film is measured by ellipsometry, as shown in Figure 2.2. Due to the same reason, the RI of ZIF-8 is also smaller than most of the commercially available substrates. The imaginary part of ZIF-8 is also zero within the measured wavelength which means no absorption caused by ZIF-8.

2.2. Surface Morphology of Metal-Organic Framework Thin Film

MOF thin film is formed by dense NPs. Therefore, the surface morphology will not be perfectly smooth as sputtered or thermally evaporated thin film. For optical devices, there are two major losses: absorption and scattering. Since we already determined that the two MOFs do not have absorption at the interested wavelength region, the next step will be determining the surface morphology of the two MOFs.

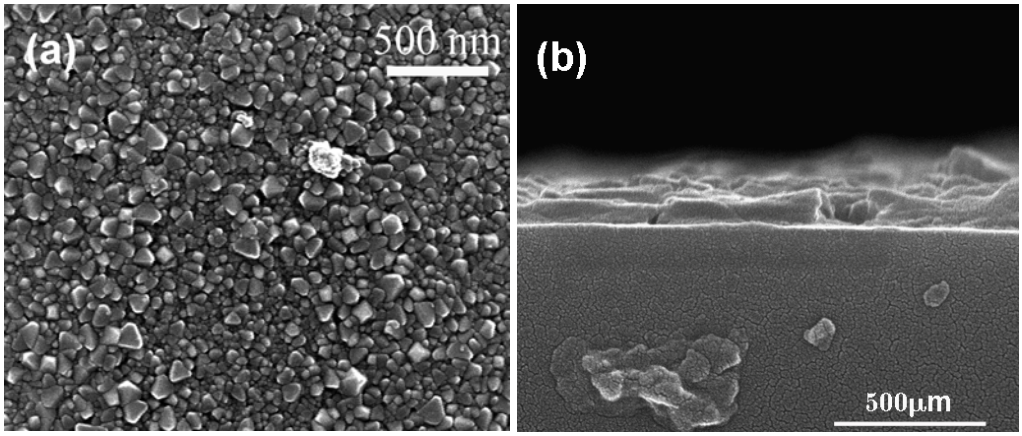

Figure 2.3 The (a) top view and (b) cross-section view of Cu-BTC thin film.

Figure 2.3(a) and 2.3(b) are the top view and cross-section view of the scanning electron microscopy (SEM) images of Cu-BTC thin film. As we can see,

the Cu-BTC NPs are densely packed on the substrate forming a thin film. There are no obvious voids on the thin film. The cross-section view was used to calibrate and growth rate and the final film thickness. To quantitively determine the roughness of the Cu-BTC thin film, the surface morphology was investigated by atomic force microscope (AFM), as shown in Figure 2.4. The root mean square of the surface profile is 64.1 nm.

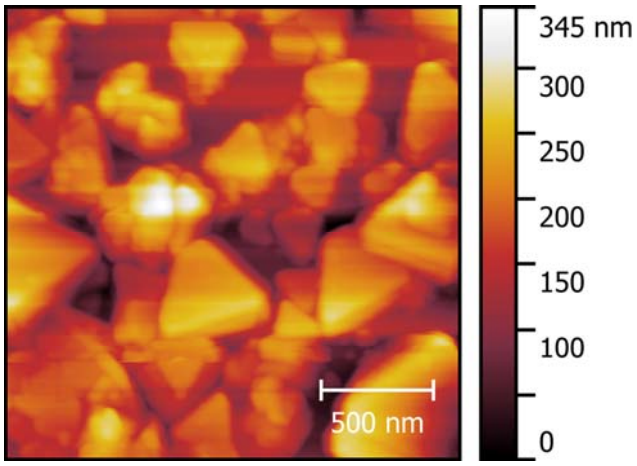

Figure 2.4. AFM image of ZIF-8 thin film.

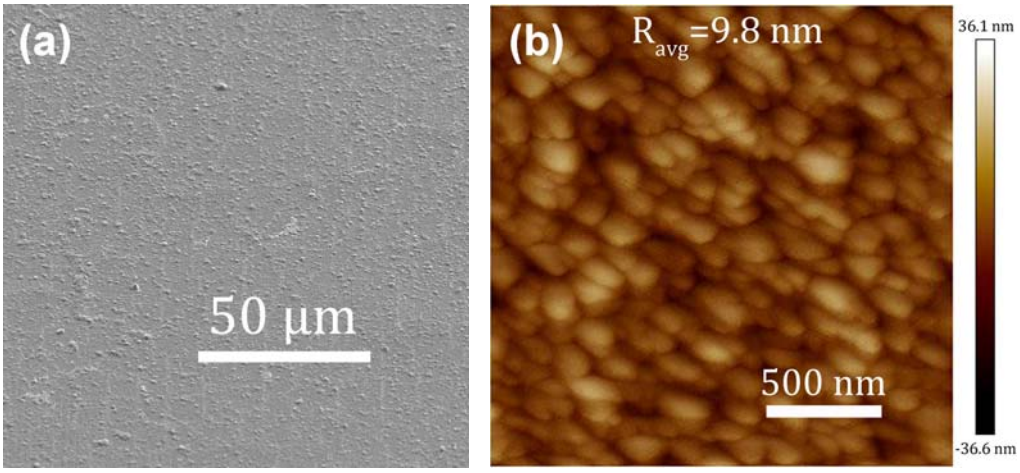

Figure 2.5. (a) SEM image and (b) AFM image of ZIF-8 thin film.

Comparing to Cu-BTC MOF, ZIF-8 thin film has much smoother surface, as shown in Figure 2.5(a). The NPs of ZIF-8 MOF is much smaller and denser. The surface roughness of ZIF-8 thin film is determined by AFM, which is only 10 nm, as shown in Figure 2.5(b).

2.3. Summary

In conclusion, the optical property and the surface morphology of two MOFs used in this work were studied. The RI of both MOFs are relative small due to the high porosity nature. The real part of the RI of both MOFs is around 1.3, which is lower than most of the commercially available substrates. Besides, both MOFs show no absorption at the interested wavelength range, which will not interfere the CO_2 gas absorption. The surface roughness of both MOFs is determined to evaluate the loss due to the scattering. Cu-BTC MOF has higher surface roughness about 64 nm, while the ZIF-8 MOF's roughness is only 10 nm. These parameters are very important for the device design and the analysis of the device performance.

CHAPTER 3. ULTRA-SHORT NEAR-INFRARED FIBER-OPTIC GAS SENSOR USING METAL-ORGANIC FRAMEWORK

In order to demonstrate the capability of MOF being used in gas sensor, in this chapter, an ultra-short NIR fiber-optic gas sensors for CO_2 detection by depositing a thin layer of MOF on the core of fiber is presented. In this NIR fiber-optic sensors, the 100 nm thick Cu-BTC MOF film coated at the surface of the fiber core absorbs CO_2 in the ambient environment, and effectively increases the local CO_2 concentration at the surface of the optical fiber, which essentially enhances the interaction between the evanescent field and the gas analyte. As a result, we successfully increased the NIR detection sensitivity with an ultra-short length of optical fiber.

3.1. Overview of optical fiber based sensor

Optical fiber sensors are playing significant roles in many engineering applications due to the unique advantages such as light weight, low cost, compact size, immunity to electromagnetic interference, high sensitivity, large bandwidth and remote sensing capability. In the past four decades, various technologies have been developed for measuring a number of different physical parameters, such as strain[108, 109], temperature[110, 111], pressure[112, 113], current[114, 115], voltage[116, 117], gas[23, 25, 118, 119], chemical [120, 121], rotation[122, 123],

vibration[115, 124], acceleration[125, 126], bending[127, 128], torsion[122, 129, 130], displacement[126, 131, 132], etc.

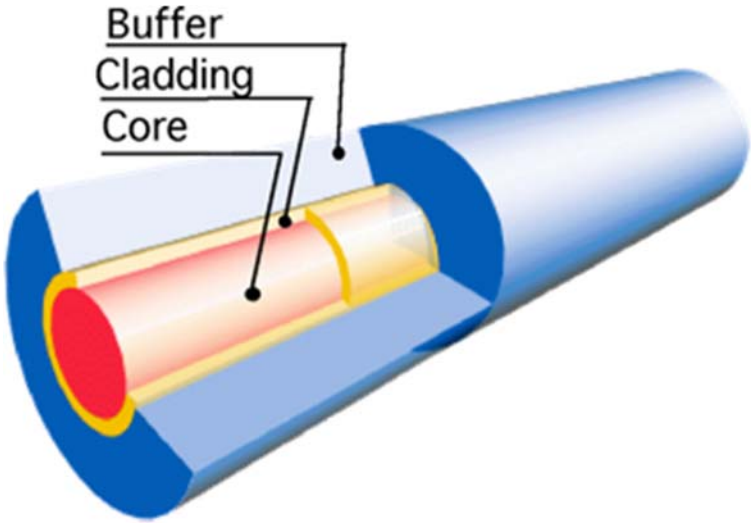

Figure 3.1. Schematic of an optical fiber[133].

An optical fiber is an optical waveguide generally made of glass. It is composed of three parts: core, cladding, and coating or buffer. The size of fibers can be very different. The most common cladding diameter is 125 μm, while the core size ranges from 10 to 50 μm. The basic structure of an optical fiber is shown in Figure 3.1. The core material has a refractive index lower than the cladding layer. Therefore, light propagates along the core based on total internal reflection. The cladding decreases the loss of light from core into the surrounding air and scattering at the surface of core. It also protects the fiber from absorbing surface contaminants,

and adds mechanical strength. The coating or buffer is a layer used to protect the optical fiber from physical damage, usually made of plastic material.

The sensors are generally based either on measuring an intensity change or on the phase changes caused by interference. Thus, they can be categorized into either intensity sensors or interferometric sensors. Techniques used based on intensity sensors include light scattering, spectral transmission changes, micro bending or radioactive losses, reflectance changes, and changes in the modal properties of the fiber. Interferometric sensors have been demonstrated based upon the magneto-optic, the laser-Doppler, or the Signac effects[134]. Among all the application, gas spectroscopy sensing is of great interests because of the importance and wide application, such as industrial production (e.g., methane detection in mines), automotive industry (e.g., detection of polluting gases), medical applications, indoor air quality monitoring and environmental studies[26]. The most common approach is evanescent field sensor. Since this sensing mechanism relies on the penetration of the evanescent field of a total internally reflected light into the absorbing medium, it suffers low sensitivity due to the small percentage of the optical power carried by the evanescent field. This issue becomes even worse for gas sensing due to the low molecule density. Compared with infrared (IR) absorption through a gas cell, the sensitivity of an equivalent length evanescent field fiber-optic sensor is typically three to four orders of magnitude lower. To resolve this challenge, we combine the optical fiber with MOF. The MOF film coated at the surface of core adsorbs gas and effectively increases the local gas

concentration at the surface of the optical fiber, which essentially enhances the interaction between the evanescent field and the gas molecules.

3.2. Fiber-Optic Gas Sensor Fabrication

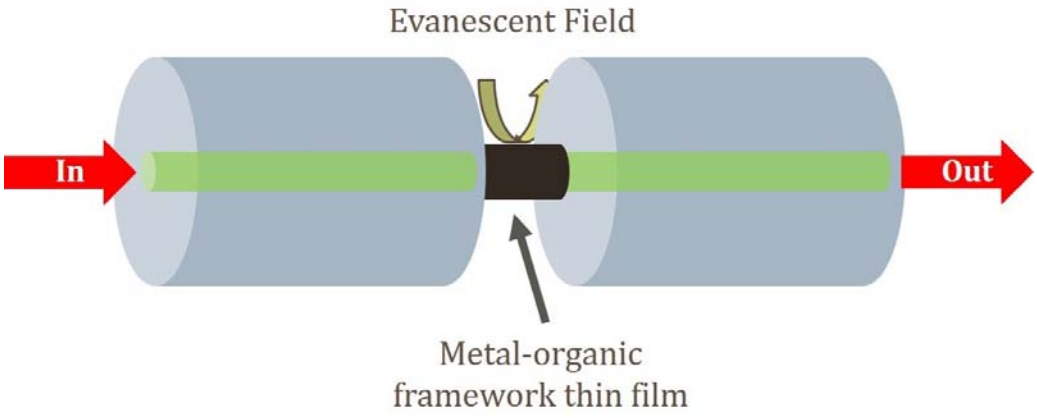

Figure 3.2. Schematic of MOF coated optical fiber gas sensor.

The fiber-optic sensor was fabricated by growing nanoporous Cu-BTC MOF on the surface of the core of an optical fiber. Briefly, a 1 m long optical fiber was fixed on a silicon substrate by UV epoxy after removing the polymer coating layer by flame. Standard buffered oxide etchant (BOE) was then used to etch away the cladding layer of the optical fiber by immerging the silicon substrate into the BOE solution. During the etching process, the fiber was connected to a 1.55 μm laser diode and an optical power meter was used to monitor the optical transmission through the optical fiber. When the transmitted optical power dropped 1.5~2 dB, the etching process was stopped by taking out the silicon substrate from the BOE and rinsing with deionized water.

MOFs were grown on both the surface of etched region of optical fiber and a piece of sapphire substrate by layer-by-layer (LBL) method[135], as shown in Figure 3.2. The optical fiber was first treated by oxygen plasma and then immersed in a 300 mL ethanol solution which contains 10 mM metal precursor $Cu(OAc)_2$ for 20 min. Subsequently, the optical fiber was immersed in another 300 mL ethanol solution which contains 1 mM organic ligand BTC for 40 min. Between each step, the fiber was rinsed with ethanol to remove the unreacted precursor ions or molecules to ensure the uniform growth and then naturally dried at room temperature (295.5 K) for 10 minutes. Cu-BTC MOF thin film on optical fiber was grown by 40 cycles LBL method.

For comparison, bulk Cu-BTC synthesized via a typical solvothermal method in a batch reactor was also prepared. A solution of $Cu(NO_3)_2$ (3.6 mM) in 60 mL of ethanol and BTC (8.1 mmol) in 60 mL of ethanol were both stirred for 10 min in a 250 mL beaker, separately. A 50/50 mixture of $Cu(NO_3)_2$ and BTC solution was stirred for 10 min, then was placed in a Teflon autoclave. The sealed autoclave was heated to 120 °C, held for 18 h in a convective oven, and cooled to room temperature naturally. The collected reaction products were washed with ethanol 3 times and were dried under vacuum for 24 h at 70 °C. Nitrogen sorption/desorption isotherm was measured at -196 °C with a Micromeritics ASAP 2010 analyzer. The samples were degassed in vacuum for 2 h at 150 °C prior to analysis. The Brunauer-Emmett-Teller (BET) surface areas were obtained from the amount of N_2 physisorbed at different relative pressures (P/P_0), based on the linear part of the 6

points sorption data at P/P_0 = 0.02 - 0.10. The total pore volume was calculated by the Horvath Kawazoe method at P/P_0 = 0.99. The mesopore volume and micropore volume were obtained by the Barrett-Joyner-Halenda sorption and the t-plot methods, respectively. The pore size distribution was evaluated by the original density functional theory model.

3.3. Experimental Demonstration

3.3.1. Multi-Mode Optical Fiber Based Sensor

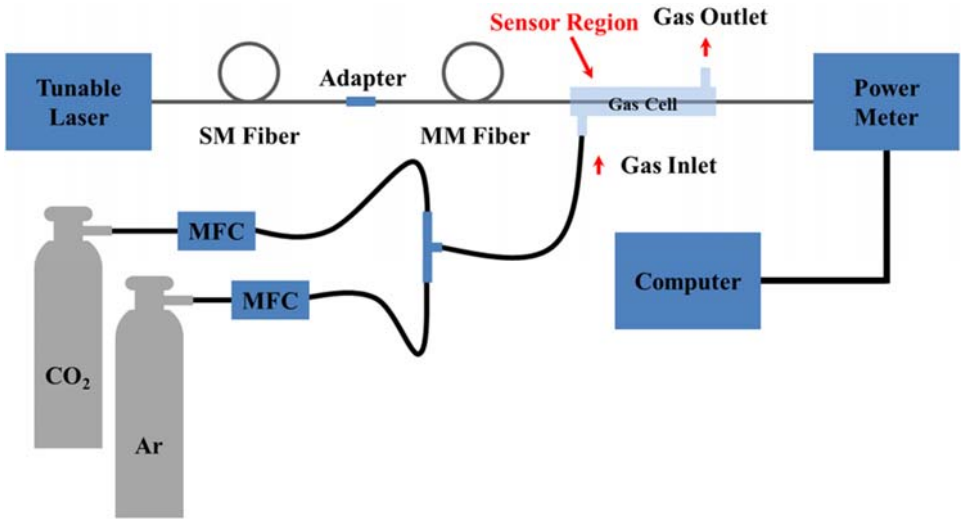

Figure 3.3. Schematic of the experiment setup for CO_2 sensing.

The first MOF coated optical fiber based gas sensor was made by multi-mode fiber (MMF). A fluorine-doped silica cladded/silica core MMF (Thorlabs AFS 105/125Y) was used, which has about 8 cm etched region. The experiment setup for CO_2 sensing is shown in Figure 3.3. A tunable semiconductor laser diode (HP 8168) with a standard single mode (SMF28) fiber pigtail was used as the light

source. The output light was first split by a 1×2 10:90 coupler. 10% of the light was coupled into a power meter (Thorlabs, Inc. PM20) as the reference, and the other 90% was coupled into the fiber-optic sensor by a buffered fiber adapter (FIS F18294). The sensor was placed inside a gas cell, which was connected to the CO_2 and Ar gas tanks. The transmitted light through the sensor was directly coupled to another power meter (Thorlabs, Inc. S122C), and the data was collected by a personal computer through a USB power and energy meter interface (Thorlabs, Inc. PM100USB). Gas flows were controlled by two mass flow controllers (MFC) (Aalborg, GFC 17) with 0-20 ml/min flow range. Different CO_2 concentration was achieved by varying the mixing ratio of CO_2 and Ar flows.

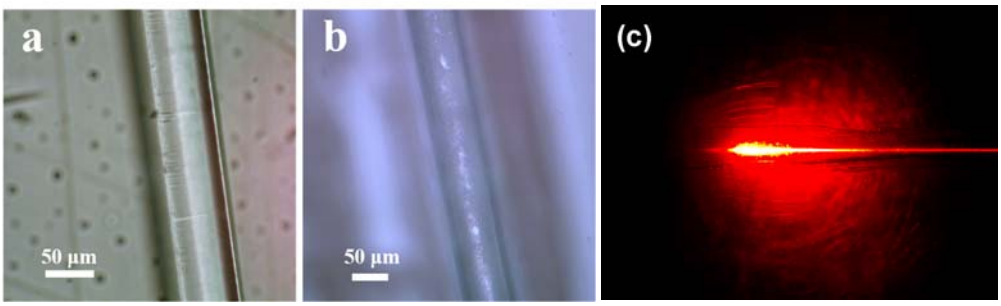

Figure 3.4. Optical images of etched fiber (a) before and (b) after coating MOF. (c) Optical scattering image of the MOF-coated fiber illuminated by a 635 nm red laser.

Before conducting the CO_2 sensing experiment, the device was first characterized. Optical microscopy images of the optical fiber before and after growing Cu-BTC MOF are shown in Figure 3.4 (a) and 3.4(b). The silica core of the optical was coated with MOF which shows a light blue color due to the copper ions. The optical image of the MOF-coated optical fiber illuminated by a 635 nm

semiconductor laser in Figure 3.4(c) confirms the strong optical scattering of Cu-BTC MOF.

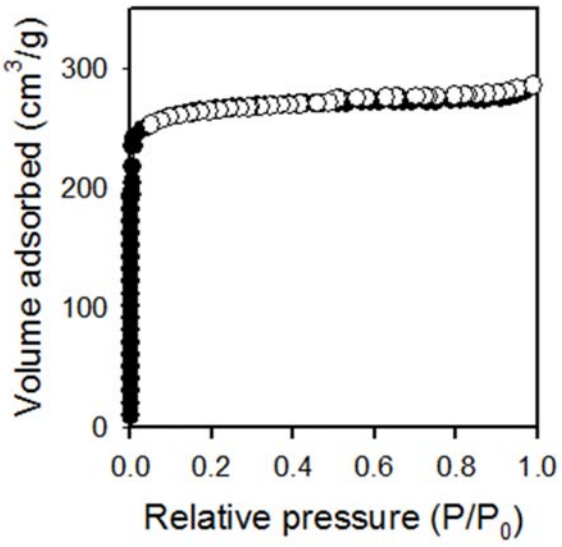

Figure 3.5. N_2 gas isotherm of the bulk Cu-BTC MOF.

Table 3.1. Texture properties of the Cu-BTC MOF bulk and thin film

Cu-BTC bulk				Cu-BTC film			
S_{BET} (m^2 g^{-1})[a]	Pore volume (cm^3 g^{-1})			Thickness (nm)	Length (cm)	Volume[e] (um^3)	Surface area (m^2)[f]
	V_{total}[b]	V_{meso}[c]	V_{micro}[d]				
886	0.441	0.078	0.364	100	5	$3x10^6$	$0.93x10^{-3}$

[a]BET surface area. [b]Total pore volume. [c]Mesopore volume. [d]Micropore volume. [e]Total volume of MOF film on fiber. [f]Estimated from S_{BET} of bulk Cu-BTC.

Figure 3.5 shows the N_2 gas sorption-desorption isotherm of the bulk Cu-BTC MOF. Isotherm shows a typical characteristic of microporous materials rapidly increased at a lower P/P_0, with a small hysteresis loop associated with capillary condensation in the mesoporous structures, most probably from intra agglomerate voids in the particle. Physical properties of Cu-BTC MOF bulk and thin film are summarized in Table 3.1. The estimated surface area of the Cu-BTC thin film on the surface of SMF fabricated in this work was 0.93×10^{-3} m^2.

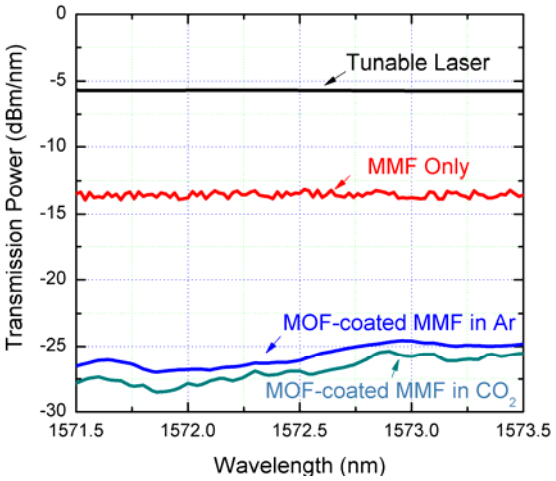

Fig. 3.6. Optical transmission spectra of the tunable laser, MMF, MOF-coated MMF in Ar and in CO_2, respectively.

To test the performance of the sensor, the gas cell was first purged by ultra-pure Ar for 2 hours to remove water vapor inside the MOF. Then, the gas flow was switched from pure Ar to CO_2 with a flow rate of 5 sccm for 5 minutes. The wavelength of the tunable laser was continuously scanned from 1571.5 nm to 1583.5 nm with 0.02 nm resolution. The optical transmission spectra of the tunable laser, MMF fiber only, MOF-coated MMF fiber with pure Ar and with pure CO_2 were plotted in Figure 3.6. Compared with the tunable laser, the MMF without MOF had 8 dB optical insertion loss due the optical coupling at the fiber connectors and the optical scattering caused by surface roughness at the sensing region. Also, the spectrum was no longer flat and smooth due to the modal noise of MMF. After coated with MOF and purged with Ar, the optical loss further increased to 21 dB due to extra optical scattering by MOF. When switched the gas flow to pure CO_2,

the optical transmission spectra dropped around 1 dB due to the CO_2 absorption. As a comparison, if the MMF is not coated with MOF, switching Ar to CO_2 will not induce any observable change of the optical transmission since the fiber is not long enough to induce detectable NIR absorption.

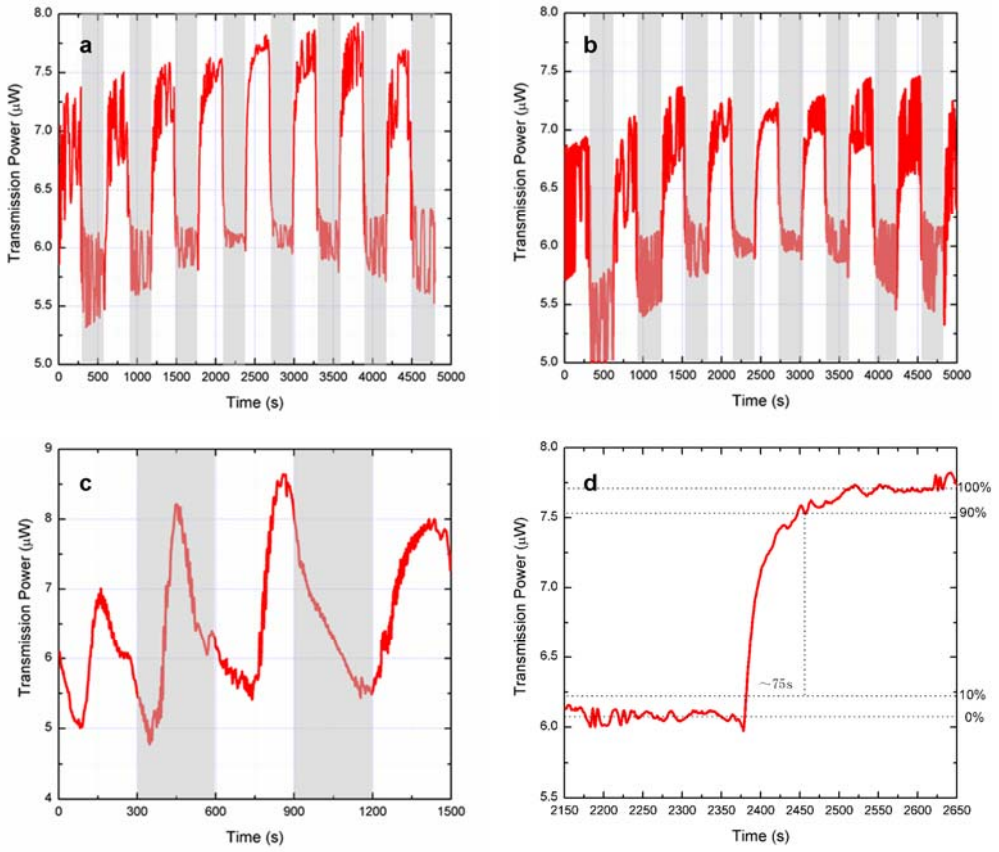

Fig. 3.7. Real-time response of the fiber-optic sensor to alternating Ar and CO_2 flows at (a) 1572.5 nm, (b) 1500 nm; Response time of the fiber-optic sensor for (c) absorbing and (d) desorbing CO_2.

To further study the dynamic response, real-time data of the fiber-optic sensor was measured. The wavelength of the tunable laser was fixed at 1572.5 nm. Then, pure Ar and CO_2 gas flows were switched alternately every 5 minutes. In Figure 3.7(a), the grey regions and white regions represent the time slots when CO_2 and Ar flows, respectively. The average transmission power difference between flowing Ar and CO_2 is about 1.6 μW. As a comparison, the absorption measurement was repeated at 1500 nm in Figure 3.7(b) with average absorption around 1.1 μW. This observation implies that the absorption spectrum of CO_2 in MOF might be different from the gas in free space, which should have orders of magnitude higher absorption rate in the 1572.5 nm absorption lines than in 1500 nm. Interestingly, when we used 635 nm laser diode as the light source, we did not observe any meaningful absorption. Our results confirmed that the optical absorption at 1572.5 nm and 1500 nm were caused by the CO_2 absorption in MOF, which may have different spectral widths than the few narrow lines as predicted by HITRAN. The response time of the sensor was measured for both the absorption and desorption process as shown in Figure 3.7(c) and (d). The absorption time (from 90% to 10%) was approximately 40 seconds and the desorption time (from 10% to 90%) was approximately 75 seconds. It should be noticed that these results the overall response times including purging the gas cell with volume of 7 cm^3. The MOF layer is only 100 nm thick, and the absorption time and desorption time for CO_2 is therefore likely to be negligible compared with the time to purge the gas cell.

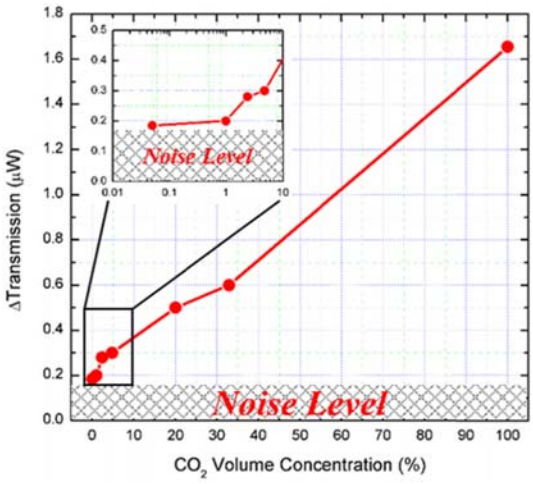

Fig. 3.8. Average ΔTransmission as a function of CO_2 volume concentration in Ar. Inset: zoomed-in plot for low concentration (log scale).

The detection limit of the fiber-optic sensor was tested by measuring the change of the transmitted optical power (ΔTransmission) as a function of CO_2 concentration. Different CO_2 concentrations were obtained by controlling the flow rates of pure Ar and CO_2. From the plot of Figure 3.8, we can clearly observe the relation between ΔTransmission and the CO_2 concentration. The slope at higher concentration (>5%) is smaller than that at lower CO_2 concentration. This is because higher concentration CO_2 will saturate the nanoporous MOF film, which is consistent with the reported results[136]. The inset figure shows zoomed-in plot of ΔTransmission vs. CO_2 volume concentration in log-scale. The lowest CO_2 concentration we measured is 500 ppm, which is limited by the noise of the MMF, which caused signal fluctuation that is comparable with low concentration CO_2

absorption. Using a single-mode optical fiber coated with MOF should further improve the detection limit.

3.3.2. Single-Mode Optical Fiber Based Sensor

Previously, we developed an ultra-short NIR fiber-optic CO_2 sensor through Cu-BTC MOF thin films to enhance the intrinsically low sensitivity of NIR spectroscopy. The proof-of-concept has been demonstrated by an 8-cm long multimode fiber (MMF) sensor coated with 100 nm thick Cu-BTC MOF thin film. However, many fundamental issues related to the sensing mechanism of CO_2 in MOF have not been revealed, and the detection limit of 500 ppm is still above the CO_2 concentration in the ambient atmosphere. In order to solve these issues, we prepared Cu-BTC MOF thin films on standard single-mode fibers (SMFs) to enhance the sensitivity.

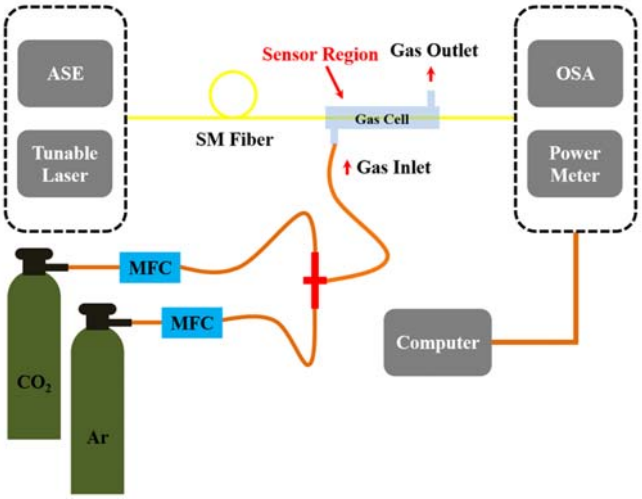

Figure 3.9. Schematic of the experimental setup for CO_2 sensing used in this study. ASE: Amplified spontaneous emission; OSA: Optical spectrum analyzer; MFC: Mass flow controller.

The experimental setup for CO_2 sensing is shown in Figure 3.9, which is slightly different from the MMF based sensor. A tunable semiconductor laser diode (HP 8168) and an amplified spontaneous emission (ASE) light source (Thorlabs, Inc. S5FC1550S-A2) were used to couple light into the fiber-optic sensor by fusion splicing another SMF with the gas sensor. Fusion splicing improved the coupling stability by 20 dB compared with optical coupling using 3-axis stages and therefore enhanced the signal-to-noise ratio (SNR). The gas sensor was placed inside a gas cell, which was connected to CO_2 and Ar gases. The transmitted light through the sensor was directly coupled to a power meter (Thorlabs, Inc. S122C) or an optical spectrum analyzer (Thorlabs, Inc. OSA203), and the data were collected by a personal computer. Flow rates of gas were controlled by mass flow controllers (MFC) (Aalborg, GFC 17) with 0-20 mL min-1 flow range. Different CO_2 concentration was achieved by varying the mixing ratio of CO_2 and Ar flows.

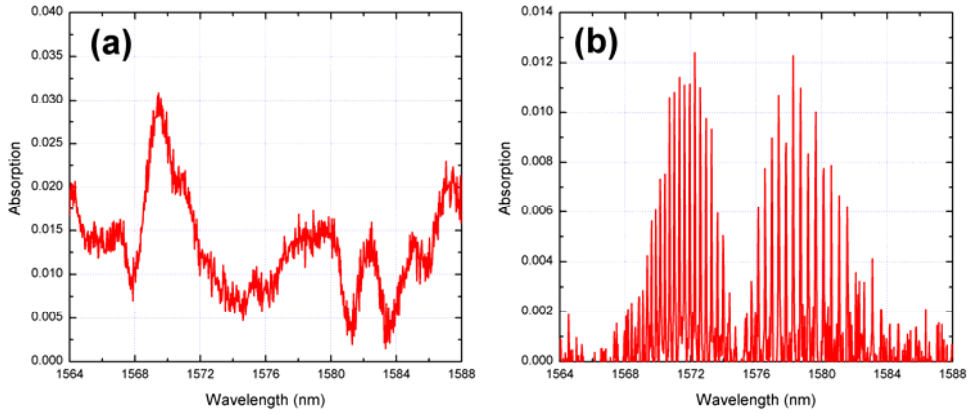

Figure 3.10. Absorption spectra of (a) CO_2 bound inside MOF and (b) gas phase CO_2 inside quartz gas cell.

ASE light source and OSA were used to obtain the absorption spectrum for the MOF-coated SMF sensor. Prior to the measurement, the sensor was purged with pure Ar gas for 12 hours to remove all the gas molecules, especially the water vapor inside the porous structures. After that, the transmission spectrum was collected as the reference. Then, the gas flow was switched from pure Ar to pure CO_2. The transmission spectrum was collected when it became stable. The absorption spectrum was calculated based on Beer-Lambert law and is shown in Figure 3.10(a). As a comparison, the absorption spectrum of gas phase CO_2 in a 10 cm quartz gas cell (PIKE Technologies Inc. 162-1810) was also measured, as shown in Figure 3.10(b). For gas phase CO_2, it exhibited both vibrational bands and rotational fine lines which matched with the theoretical results from HITRAN database. However, for CO_2 adsorbed MOF film, unlike the gas phase CO_2, a broad absorption peak between 1568 nm ~ 1572 nm was observed. The missing rotational fine lines of the absorption spectrum was attributed to energy transition change of the rotational states caused by the bonding effect of the gas molecules inside the MOF pores. The discrepancy of the peak position of these two spectra can also possibly be caused by the interaction between CO_2 molecules and sorption sites in MOF[137]. Besides, the multiple peaks between 1576 nm and 1588 nm should be the other vibrational band at 1576 nm ~ 1583 nm, since these peaks are repeatable in the experiments. However, we still do not fully understand why the absorption peak splits into multiple peaks and why these absorption peaks are weaker than the one at 1568 nm ~ 1572 nm. It is possible that the bonding state also changed the symmetry of the

vibrational bands. Further quantitative investigation will be conducted in the future work.

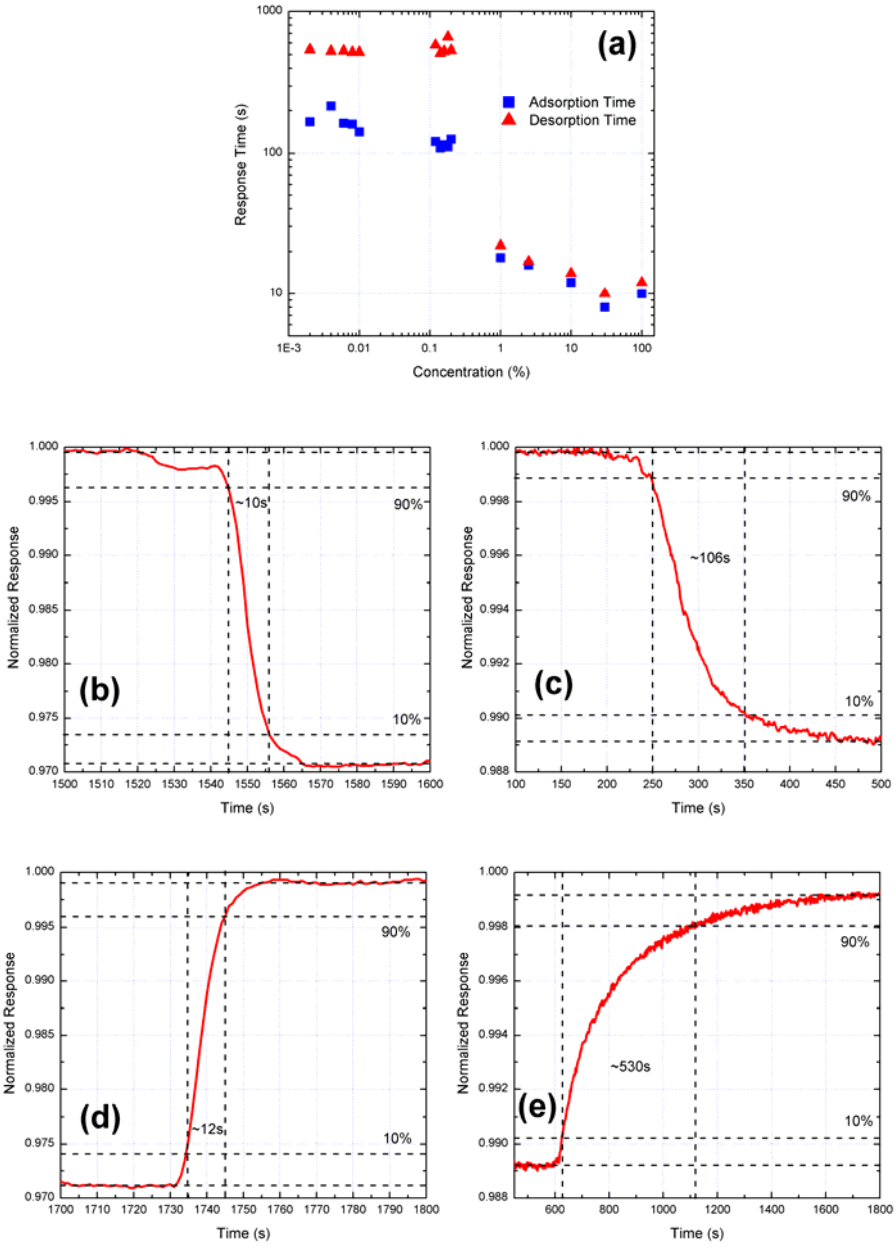

Figure 3.11. Dynamic responses of the MOF-coated SMF sensor for alternating pure Ar and CO_2 – containing flows: (a) sorption time and desorption time as a

function of CO_2 concentration; (b,c) sorption time and (d,e) desorption time for pure CO_2 and 30 ppm CO_2, respectively.

To investigate the dynamic response of the sensor, the light source and detector were changed to a tunable laser diode and a power meter. The wavelength of the tunable laser was fixed at 1569 nm, which is the absorption peak of CO_2 in MOF as shown in Figure 3.10 (b). The real-time response was studied by monitoring the transmission power when switching pure Ar and CO_2 flows alternatively. As shown in Figure 3.11(a), the response time for low and high concentration CO_2 are significantly different. At low concentration, both sorption and desorption time are much longer than that of at high concentration CO_2. Figures 3.11(b) and 3.11(d) show the optical transmittance of CO_2 during sorption and desorption processes with 100% CO_2 and 100% Ar flowing. It can be seen that at high concentration, the sorption (from 90% to 10%) and desorption time (from 10% to 90%) are 10 seconds and 12 seconds, respectively. However, at low concentration (30 ppm CO_2 in Ar), both processes become much slower as shown in Figure 3.11(c) and 3.11(e).

This significant difference can be explained by different sorption and desorption kinetics at high and low CO_2 concentration[138-140]. At high concentration, most of the gas molecules are physically adsorbed inside the MOF pores. Due to the relatively small activation barrier of physisorption, the sorption and desorption rate can be very fast, which is determined by the concentration

gradient. Moreover, the process is reversible, as shown in Figure 3.10 (b) and 3.10 (d). On the other hand, at low concentration CO_2, chemical bonding becomes dominant instead of physical bonding. This chemisorption behavior inside Cu-BTC pore is expected to be complicated, since there are three sorption sites exhibiting different interaction energy: (1) unsaturated metal site (UM), (2) tetrahedral cage opening site (TCO) and (3) center of tetrahedral cage site (CTC)[141]. The most stable site is the UM site (sorption energy: -28.2 kJ mol-1), where CO_2 molecules interact with Cu^{2+}. The TCO and CTC are less stable than UM sites, whose interaction energies are almost the same, about 5 kJ mol^{-1} less stable than UM sites. When CO_2 is flowed, CO_2 molecules are preferentially first adsorbed on the twelve UM sites in a unit cell. Only after all the UM sites are occupied (CO_2:Cu^{2+} ratio > 12:12), TCO sites will start to sorb gas molecules. When the CO_2:Cu^{2+} ratio is greater than 20:12, CTC sites will start to sorb gas molecules. If the concentration is even higher, the large pores will also start to sorb CO_2 molecules in the pores. Although bonding energy will not act as an activation barrier, the sorption activation barrier for chemical bonding is still higher than physical bonding, which will lead to a longer response time. For the desorption process, since certain amount of energy is required to break the chemical bonding and release the CO_2 molecules, therefore longer response time are needed.

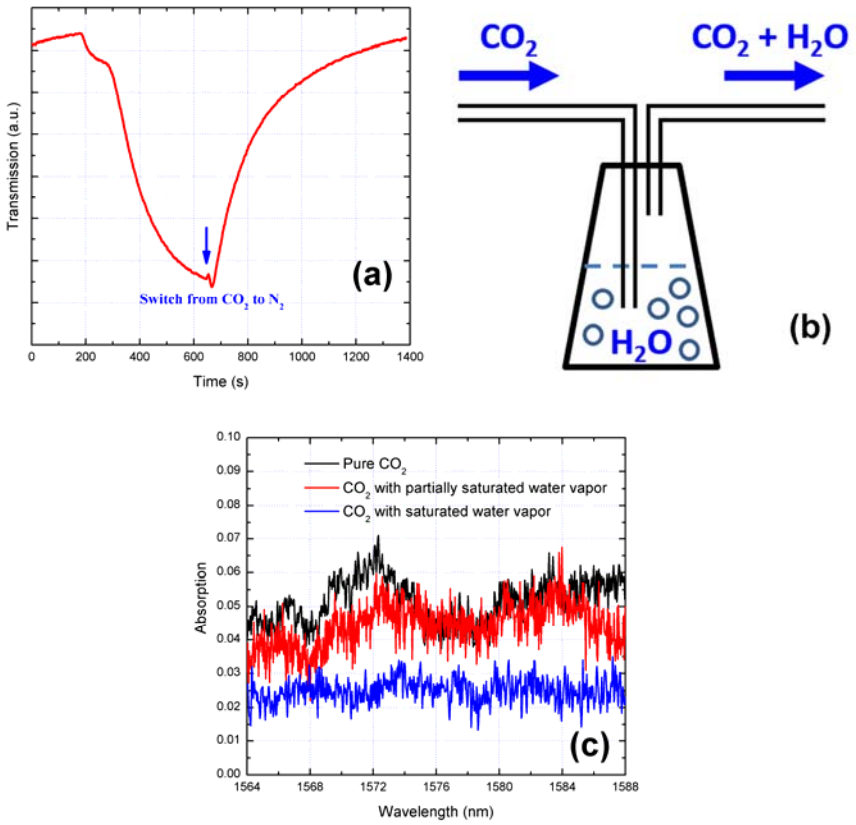

Figure 3.12. (a) Response time of the SMF sensor when purged by pure N_2 and CO_2. (b) Setup for mixing water vapor with CO_2. (c) The absorption spectra of CO_2 with and without vapor.

For real gas sensing, the interference from other gases such as nitrogen (N_2) and water vapor cannot be ignored. In this paper, the effect of these two most significance gases were also studied. The experiments are conducted under room temperature (295.5 K). For N_2, the purging gas was changed from Ar to N_2, and the response of the sensor for pure (100%) CO_2 is shown in Figure 3.12(a). Compared

to Ar, the response time of N_2 purging became much longer. Unlike Ar which is not adsorbed by MOF at all, N_2 can still be adsorbed in MOF pores, although the adsorbing affinity is lower than CO_2. Therefore, after purging with N_2, some of the pores in MOF will remain occupied. When changing the flow gas to CO_2, the CO_2 gas molecules have to repel the N_2 molecules in the pores, which results in a much longer response time. For real engineering applications, neither Ar nor N_2 purging are efficient methods. To quickly reset the SMF gas sensor, heating and/or vacuum are anticipated to be a better way to release the adsorbed CO_2 from the MOF pores.

Water vapor is another major interference since the sorption affinity to MOF is much higher than CO_2. Especially for Cu-BTC, which is hydrophilic, both theoretical and experimental investigations have shown a strong affinity of water molecules[142, 143]. The effect of water vapor is qualitatively studied using a simple setup shown in Figure 3.12(b). Briefly, pure (100%) CO_2 gas passes through a water bath before entering the gas cell. If the inlet gas tube is immersed below the water surface, water vapor close to the saturation pressure at room temperature will be mixed with CO_2. If the inlet gas tube is placed above the water surface, water vapor pressure in the mixed gas will be less than the saturation pressure. The spectral response of the sensor is shown in Figure 3.12(c). It is seen that adding water vapor into the CO_2 flow will drastically alter the sensor response. Due to the competitive sorption between CO_2 and water vapor, more water vapor is taken by MOF and occupies most of the sorption sites. Therefore, the amount of CO_2 molecules that can be adsorbed by MOF is significantly reduced. In addition, the

NIR absorption coefficient of water vapor at 1.57 μm is about two orders of magnitude lower than that of CO_2 according to HITRAN database. As a result, the CO_2 absorption band becomes less observable and the overall NIR absorption is reduced as the water vapor in the CO_2 flow increases. Based on our experimental work, a desiccation process is necessary to remove the water vapor. Actually, many gas sensors suffer the interference from water vapor when working in real environment[144]. In order to eliminate the effect of water vapor, several methods have been developed, such as silica gel desiccant dryer[145], thermoelectric cooler[146] and vapor separation membrane[147-149]. Among them, the Nafion membrane has the best performance and is widely used for water vapor separation. Therefore, for the future practical application, a Nafion membrane can be used to wrap around the gas sensor to remove the water vapor, which is very straightforward.

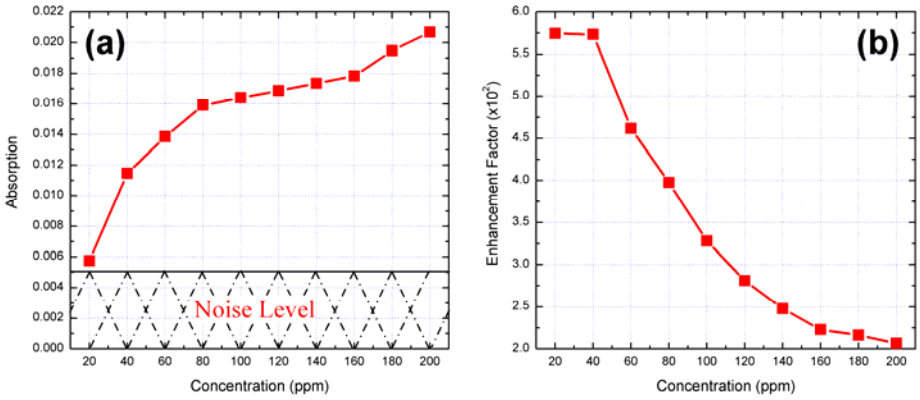

Figure 3.13. (a) Average absorption and (b) enhancement factor as a function of CO_2 volume concentration in Ar.

The detection limit was studied by measuring the change of the transmission power as a function of CO_2 concentration. Different CO_2 concentration was controlled by diluting with Ar. As shown in Figure 3.13(a), the lowest concentration that can be detected was about 20 ppm, which is one order lower as compared with the previously reported MOF-coated MMF sensor[150]. The enhancement factor γ was calculated based on the Beer-Lambert law, as shown in Figure 3.13(b). The γ is not a linear function of CO_2 concentration, and is larger at lower concentration. Usually, the evanescent field optical sensors have lower γ (<1) due to the weaker light-matter interaction. However, MOF can concentrate CO_2 inside the pores resulting in a much higher CO_2 molecule than the ambient environment. Therefore, the actual γ (>1) is the combined result of evanescent field and CO_2 concentration effect in MOF pores.

Table 3.2. Key parameters of the sensor

Detection Limit (ppm)	FOM (ppm·cm)	Noise Level (μW)*	Response Time (s)	Sensor Length (cm)
20	100	~ 0.2	8 ~ 625 / 10 ~ 710	5

* Above the noise level, the power change of the transmission light due to the absorption can be detected.

Here we define the figure-of-merit (FOM) = sensitivity × optical pathlength. Therefore, the FOM of our gas sensor is 100 ppm·cm. D. Sonnenfroh et al.[151] reported CO_2 sensor with 0.09 ppm sensitivity using a 20 cm integrated cavity at 2.0 μm wavelength. However, the actual optical length reaches ~50 m which results

in FOM = 450 ppm·cm. Besides, the absorption coefficient at 2.0 μm is about 70 times higher than that of at 1.57 μm. E. Hawe et al.[152] used an integrating sphere to achieve 200 ppm sensitivity. The optical length is 114 cm which gives FOM = 2.28 × 104 ppm·cm. Compared with these recently reported NIR CO_2 sensors, our sensor shows the best FOM. Table 3.2 lists the key parameters of the sensor.

3.4. Summary

In summary, we have developed ultra-short NIR fiber-optic gas sensors based on MOF-coated optical fiber for CO_2 sensing. For the MMF based sensor, we achieved a detection limit of 500 ppm by only 8 cm sensing length, and the overall real-time response was found to be only 40 seconds for absorption and 75 seconds for desorption in a gas cell designed in this study. For the SMF based sensor, we obtain high-resolution NIR spectroscopy of CO_2 adsorbed in MOF, which indicates an interesting phenomenon that the tightly confinement gas molecules inside MOF do not show rotation side bands as they are in free space. Real-time measurement of the sorption and desorption time at low and high concentration of CO_2 further reveals the complex sorption mechanism of CO_2 in Cu-BTC MOF. Moreover, the detection limit is improved down to 20 ppm with only 5 cm sensing region.

CHAPTER 4. PLASMONIC NANO-ANTENNA INTEGRATED METAL-ORGANIC FRAMEWORK ON SAPPHIRE SUBSTRATE

In Chapter 3, we have already demonstrated the preconcentrating capability of MOF, which can be very useful for gas sensor application. In this chapter, we integrated MOF with plasmonic nanostructure to extend the SEIRA spectroscopy technique to gas sensing. A nanophotonic device consisting of plasmonic nano-patch array with integrated metal-organic framework (MOF) for enhanced infrared absorption gas sensing was proposed. By designing a gold nanopatch array (Au-NPA) on a sapphire substrate, we are able to achieve enhanced optical field that spatially overlaps with the MOF layer, which can adsorb CO_2 with high capacity. Experimental results show that this hybrid plasmonic-MOF device can effectively increase the infrared absorption path of on-chip gas sensors by more than 1,100-fold. The demonstration of infrared absorption spectroscopy of CO_2 using the hybrid plasmonic-MOF device proves a promising strategy for future on-chip gas sensing with ultra-compact size.

4.1. Theoretical Study

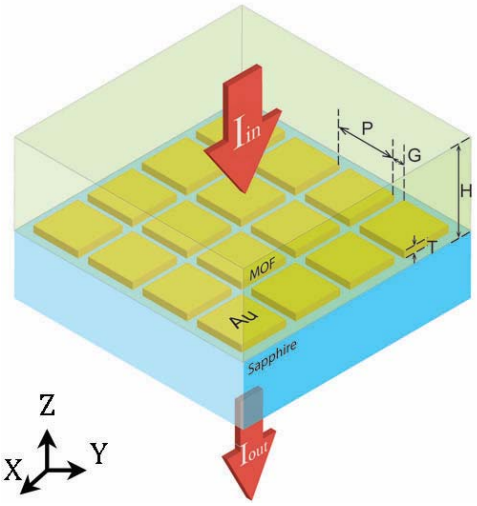

Fig. 4.1. Schematic of the MOF integrated plasmonic nanopatch array. For geometrical parameters, P is the gold nanopatch period, G is the nano-slit width, H is the MOF thickness and T is the gold thickness. Iin and Iout stand for the intensity of the incident and transmitted light.

The device consists of a gold Au-NPA on a sapphire ($n_{sapphire}$ = 1.721) substrate, which is covered by a thin layer of MOF (n_{MOF} = 1.326), zeolitic imidazolate frameworks (ZIFs) or ZIF-8, as shown in Figure 4.1. Light is launched from the MOF side, and the transmitted light is collected from the substrate. When the light is coupled into the device normal to the surface, surface plasmon resonances (SPRs) are excited at the Au/MOF interface and coupled with the Fabry–Pérot (FP) modes in the MOF layer as well. Since the Au-NPA is symmetric, the device is polarization independent. Based on the design, the parameters that can

be modified are the periodicity (P) of the Au-NPA, gap width (G) between Au-NPs, the thickness (H) of the MOF layer and the Au thickness (T). In order to achieve high optical field enhancement within the MOF layer, optimization is performed by the DiffractMOD of Rsoft photonic component design suite, which is based on rigorous coupled-wave analysis (RCWA)[153]. Among these parameters, the MOF thickness (H) is the most important one. The optical effect of the parameters is well-studied in the literature for plasmonic nano-antennas[154]. The periodicity (P) of the Au-NPA determines the peak wavelength; the gap (G) affects the transmission intensity and also the spectrum width; the Au thickness (T) also has an influence on the transmission intensity. In this paper, we focused on the detailed study of the MOF thickness (H) as it not only affects the optical field enhancement, but also determines the infrared absorption path.

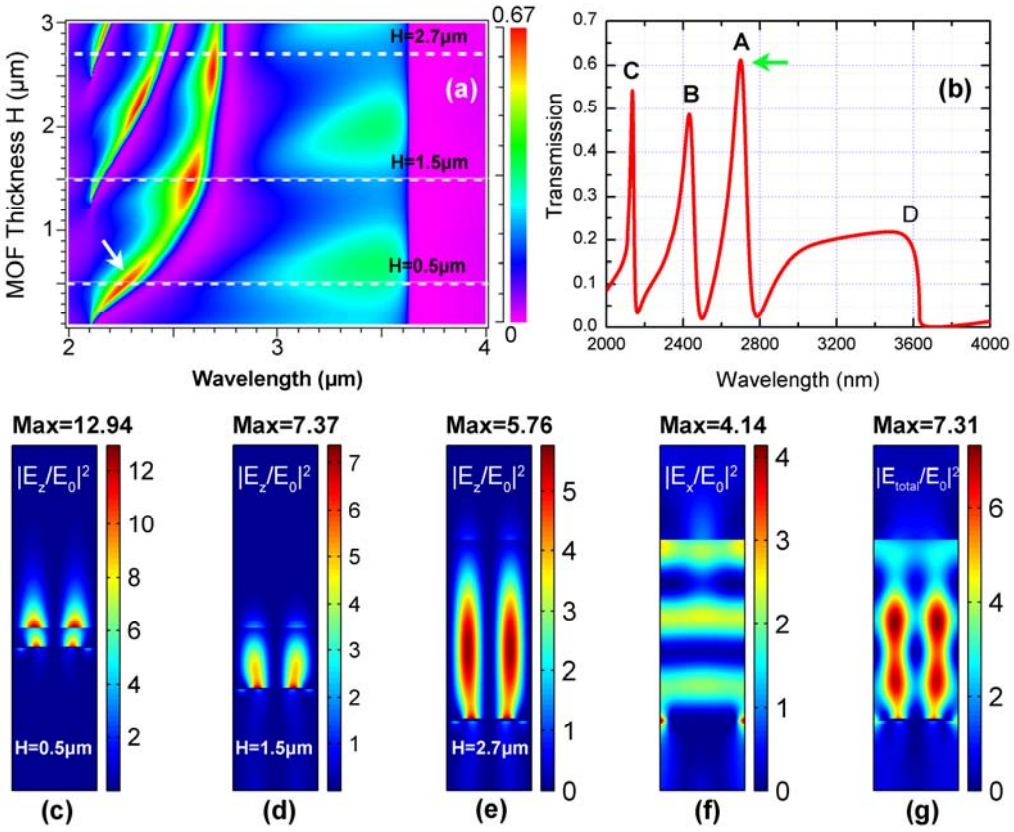

Fig. 4.2. (a) The effect of the MOF thickness H, with fixed P, T and G. The color bar represents the transmission intensity. Electric distribution of z direction for (b) H = 0.5 μm, (c) H = 1.5 μm and (d) H = 2.7 μm. (e) Simulated transmission spectrum, and the electric field distribution of (f) x direction, and (g) the summation of all directions at the peak A (λ = 2.7 μm) with green arrow.

A scanning of the MOF thickness (H) is performed by fixing other parameters. The transmission intensity results are shown in Figure 4.2(a). The major peak (indicated by the white arrow) shows a red-shift when the MOF thickness (H) increases from 0.4 μm to 3.0 μm. For real applications, the transmission intensity

should be high enough to obtain good signal-to-noise ratio. Thus, the three peaks in the simulated transmission spectrum for H=2.7 um shown in Figure 4.2(b) with over 50% transmission efficiency provide excellent measurement condition. In order to verify whether the thickness (H) is appropriate, three different values are selected from the three regions represented by the white dash lines. The electric field distributions of the three thickness at peak at 2.7 μm after modifying the period are shown in Figure 4.2(c-e). For H = 0.5 μm, it has the highest field intensity, but most of the enhanced field is in air instead of in the MOF layer, which is not preferred by gas sensing. For H = 1.5 and 2.7 μm, most of the field is confined in the MOF layer. If we only consider the plasmonic field, then H = 1.5 μm is better than H = 2.7 μm. However, we need to consider the amount of adsorbed gas by MOF in our design. In other words, a thinner MOF layer means less gas molecules are adsorbed. Therefore, the relatively thicker MOF is more desirable to allow more gas molecules to interact with the optical field. Finally, after comprehensive consideration of the plasmonic effect, MOF's adsorbing property, transmission intensity and also growth time for the MOF layer, the parameters are determined to be P = 2.11 μm, G = 250 nm, H = 2.7 μm, and T = 40 nm. The simulated transmission spectrum is shown in Figure 4.2(b), which has three resonant peaks in the shorter wavelength range and one sharp edge at the longer wavelength. Peak A is the desired coupled mode with ~ 60% transmission efficiency with a relatively higher Q-factor of 27.44. The electric field distributions at peak A are shown in Figure 4.2(e) (Ez only, corresponding to the plasmonic resonance of the Au NPA),

Figure 4.2(f) (Ex only, corresponding to the F-P resonance in the MOF thin film) and Figure 4.2(g) (total hybridized electric field). The maximum intensity enhancement is 7.31. Essentially, the coupled mode extends the highly localized plasmonic field to the entire MOF layer, resulting in an increase of the interaction between gas molecules inside the MOF and the optical field. Peak B and C are the higher modes of peak A, and the sharp edge D represents the Rayleigh anomaly at the substrate side[155].

4.2. Experimental Demonstration

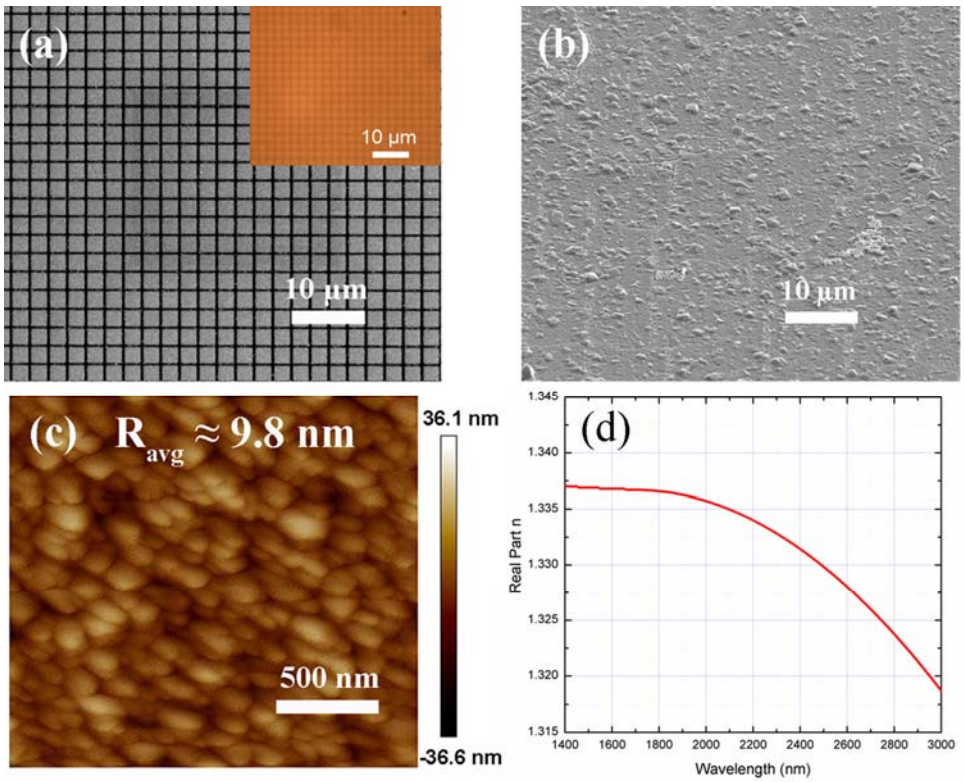

Fig. 4.3. (a) SEM image of fabricated Au- NPA. The inset is the optical image of the Au-NPA. (b) The SEM image of Au-NPA after growing MOF. (c) AFM image of the ZIF-8 thin film. (d) The refractive index of MOF thin film.

The device is fabricated by focused ion beam (FIB) etching followed by monolithic growth of a MOF thin film. The selected MOF is the zeolitic imidazolate framework-8 (ZIF-8s), which has been extensively investigated due to its excellent thermal stability and selectivity toward CO_2[156]. Besides, due to the hydrophobic surface property, water molecules can only be adsorbed at the outer surface, while CO_2 can diffuse into the inner pores. Besides, the hydrophobic surface makes ZIF-8 even more attractive for chemical sensing in environments where water vapors are pervasive[156]. The growth process is described here briefly. Before growing the ZIF-8 film, the substrate with Au-NPA is cleaned in piranha solution (H_2SO_4/H_2O_2, 70/30 v/v%) at 70 °C for 30 minute. Then it is washed thoroughly by deionized water and dried under nitrogen flow. To grow ZIF-8 thin film, the cleaned Au-NPA sample is immersed in a freshly mixed methanolic solution of 2-methylimidazole and $Zn(NO_3)_2$ for 30 min at room temperature, followed by washing using methanol and drying under nitrogen flow. To obtain 2.7 μm MOF layer, this process is repeated 32 cycles. The scanning electron microscope (SEM) images of the fabricated Au-NPA before and after growing MOF are shown in Figure 4.3(a) and 4.3(b), respectively. As we can see, the MOF layer fully covers the Au-NPA and the MOF forms a relative smooth thin film with surface roughness about 10 nm, which is measured by atomic force microscopy (AFM) as shown in Figure 4.3(c). The refractive index of MOF thin film coated on a silicon wafer was measured by elliposometry as shown in Figure 4.3(d).

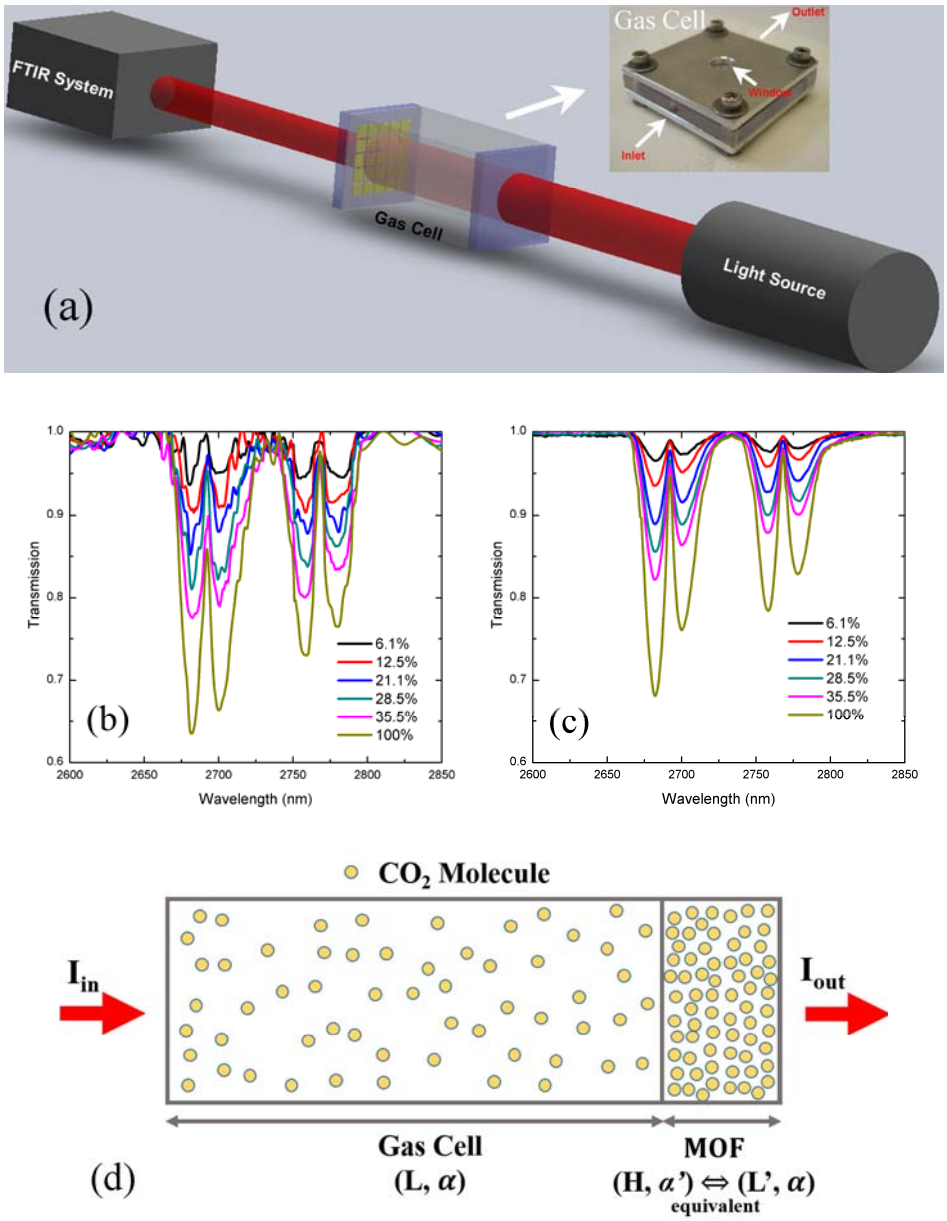

Fig.4.4. (a) Schematic of the experimental setup for gas sensing. Experimentally obtained transmission spectra of CO_2 for (b) Au-NPA coated with MOF at different CO_2 concentrations and (c) the reference. (d) Illustration of data analysis.

In order to quantitatively determine the enhancement provided by the hybrid plasmonic-MOF device, a CO_2 sensing measurement was performed by a Fourier transform infrared (FTIR) spectrometer system shown in Figure 4.4(a). The gas cell used in the system is home built with 4 mm light path length. One side of the gas cell is sealed by a sapphire window and the other side is sealed by the device. Different CO_2 concentrations are obtained by mixing with nitrogen (N_2) using two mass flow controllers. Figure 4.4(b) shows the absorption spectra of different CO_2 concentration. As a reference, the hybrid plasmonic-MOF device is replaced by bare sapphire window. As a comparison, the absorption spectra of the reference without any device are shown in Figure 4.4(c). In order to determine the enhancement provided by the device, an analysis was performed as illustrated in Figure 4.4(d). Since the reference does not have any enhancement, the absorption is purely due to the CO_2 inside the gas cell. According to the Beer-Lambert law, the absorption coefficient α of the CO_2 inside the gas cell without the hybrid plasmonic-MOF device can be calculated using the following equation:

$$I_{out} / I_{in} = \exp (- \alpha \bullet L) \tag{4.1}$$

where L is the path length of the gas cell. For the gas cell with the hybrid plasmonic-MOF device, besides the CO_2 absorption in the gas cell, there is extra IR absorption from CO_2 molecules adsorbed inside the MOF. Therefore, the total IR absorption can be expressed as:

$$I_{out} / I_{in} = \exp (- \alpha \bullet L - \alpha' \bullet H) \tag{4.2}$$

where α' is the enhanced IR absorption coefficient of the CO_2 adsorbed inside MOF layer, which is larger than α. Since the IR absorption is only exponentially proportional to the product of absorption coefficient and optical path length, Equation (4.2) can be rewritten as Equation (4.3):

$$I_{out} / I_{in} = \exp (- \alpha \bullet L - \alpha \bullet L') \quad (4.3)$$

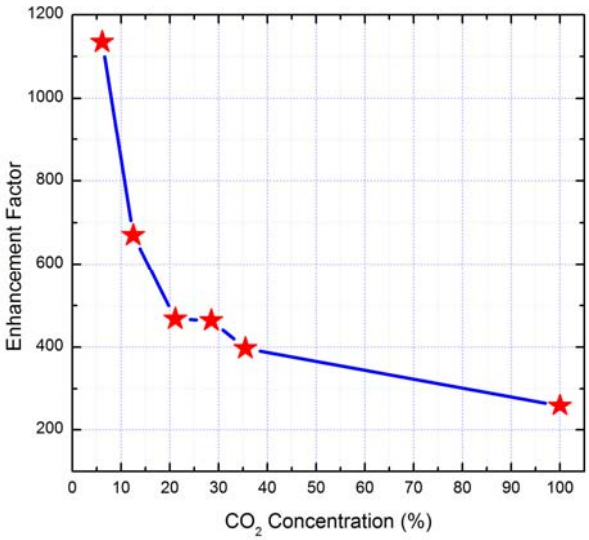

Fig.4.5. Enhancement factor of Au-NPA coated with MOF as a function of CO_2 concentration.

In Equation (4.3), L' is the equivalent optical path length provided by the plasmonic-MOF device, which has a physical length of H. Therefore, the enhancement factor (EF) is defined as EF = L'/H. The EF includes both the plasmonic field enhancement effect and also the gas concentrating effect from the MOF film. The calculated EF as a function of CO_2 is shown in Figure 4.5 using the

experimental data in Figure 4.4, with the highest EF over 1,100. The nonlinear trend is due to the nonlinear absorption behavior of MOF, which is possibly due the different adsorption mechanism at high and low CO_2 concentration as we discussed in Reference[157]. At high concentration, most of the gas molecules are physically adsorbed inside the MOF pores, which are limited by the available space. While at low concentration CO_2, chemical bond adsorption becomes dominant[23, 25], which can provide a large gas concentration factor.

4.3. Summary

In summary, we present a hybrid plasmonic-MOF device by integrating plasmonic NPA with nano-porous ZIF-8 MOF thin film. Compared with plasmonic NPs-enhanced MOF film, this new type of rationally designed nanophotonic devices provide enhanced optical transmission, higher Q-factors, stronger light-matter interaction, and tunable plasmonic resonances to match the vibrational spectra of the analytes. In this work, the hybrid plasmonic NPA-MOF thin film device was integrated with a gas cell for CO_2 sensing at 2.7 μm wavelength. Based on Beer-Lambert law, the total enhancement factor was calculated according to the experimental results. The highest EF obtained is about 1,100. This device can be applied for on-chip IR gas sensing, which can potentially reduce the absorption length of conventional gas cells by several orders of magnitude.

CHAPTER 5. PLASMONIC NANO-ANTENNA INTEGRATED METAL-ORGANIC FRAMEWORK ON SI_3N_4 MEMBRANE

In Chapter 4, we successfully applied SEIRA spectroscopy to gas sensing by integrating MOF with plasmonic nanostructure. However, most of the enhancement came from MOF's preconcentrating effect. The plasmonic effect only provided 2~3 times enhancement factor, which was majorly due to the low RI comparing to the substrate. In order to improve the plasmonic enhancement, in this chapter, we present a suspended silicon nitride (Si_3N_4) nano-membrane device integrating plasmonic nano-patch antennas with metal-organic framework (MOF), which can efficiently adsorb CO_2 through its nanoporous structure. Unlike conventional SEIRA sensing relying on hot-spots of plasmonic nanoantennas or NPs, the device in this chapter engineered the coupled surface plasmon polaritons in the metal-Si_3N_4 and metal-MOF interfaces to achieve strong optical field enhancement across the entire MOF film. We successfully demonstrated on-chip gas sensing of CO_2 with more than 1,800× enhancement factors within a 2.7 μm thin film.

5.1. Theoretical Study

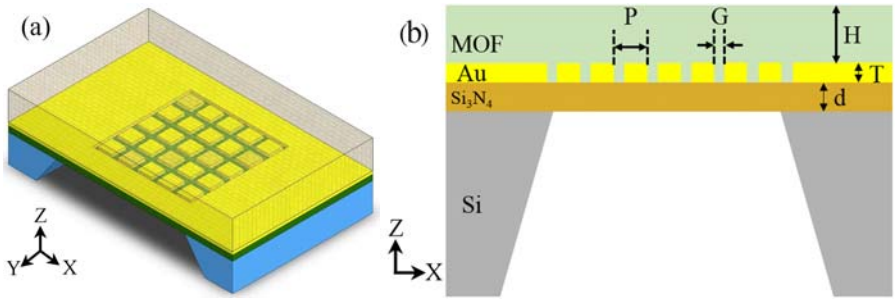

Figure 5.1. (a) Schematic of the device. (b) The cross-section of the device.

The proposed device is depicted in Figure 5.1(a), consisting of a gold nano-patch array (Au-NPA) covered by a thin layer of MOF. The whole device structure is fabricated on a Si_3N_4 nano-membrane suspended on a silicon substrate. Since the Au-NPA is symmetric in the x-y plane, the incident light is polarization independent. When light is normally irradiated onto the device, surface plasmon polaritons (SPPs) can possibly be excited at both the Au/MOF/air and Au/Si_3N_4/air interfaces. To obtain enhanced infrared absorption for gas sensing, we prefer strong light-matter interaction between the plasmonic field with gas molecules within the entire MOF layer, rather than only enhancing small volume hot-spots around the corners of plasmonic nanostructures, which has been investigated by many other groups. Previous research has shown that the optical field intensity of the SPPs at metal-dielectric interfaces is related to the RI of the substrate material[158-160], i.e. lower RI will usually result in higher plasmonic field. However, the plasmonic field at the SPPs at the Au/MOF/air and Au/Si3N4/air interfaces becomes much more complex in our suspended nano-membrane device. In this paper, we conduct in-depth study of the SPPs at the top and bottom interfaces with respect to the thickness of the MOF and Si_3N_4 film, and reveal for the first time that the interaction between theses SPPs will lead to strong cross coupling. Contrary to thick-substrate plasmonic nanostructures which prefer low-index substrate for strong localized optical field, we discover that nano-membrane Au-NPA achieves ultra-high plasmonic field enhancement near the coupling region, where the SPPs at the Au/MOF/air and Au/Si_3N_4/air interfaces form strong interference. By engineering

the coupled SPPs near the coupling region, we are able to achieve a high Q-factor of 203 to precisely match the vibrational band of CO_2 at 2.7 μm wavelength while still maintaining the peak transmission efficiency above 60%. Therefore, Au-NPA on nano-membrane shows exclusive advantages over plasmonic nanostructures on conventional glass substrates[78, 158].

In order to thoroughly study the SPP modes at both the Au/MOF/air and Au/Si3N4/air interfaces and the coupling between them, we scan the design parameters using the rigorous coupled mode analysis (RCWA) method[153]. The cross-sectional view of the device is shown in Figure 5.1(b). The parameters that can be modified in the suspended structure are the Au-NPA periodicity P, gap G, MOF thickness H, Au thickness T and the Si_3N_4 substrate thickness d. Among these geometry parameters, the plasmonic effect of Au NPA has been well-studied in the literature[154]: The periodicity P of the Au-NPA determines the peak wavelength due to the well-known extraordinary optical transmission (EOT) effect[161]; the gap G affects the transmission intensity and also the Q-factor; the Au thickness T also has an influence on the transmission intensity. The effective RI of the SPP modes on both interfaces are calculated using equation $\lambda_{spp} = n_{eff} \bullet P$ to understand the mechanism of the optimization. The thickness of the MOF film and the Si_3N_4 nano-membrane, on the other hand, determines the hybridization of the SPPs with the waveguide modes, and more importantly, affects the coupling between each other, which has not been systematically investigated. Therefore, this paper focused on optimizing the MOF thickness H and the Si_3N_4 substrate thickness d to achieve

a device with ultra-high field enhancement within the entire MOF layer while still maintaining high transmission intensity.

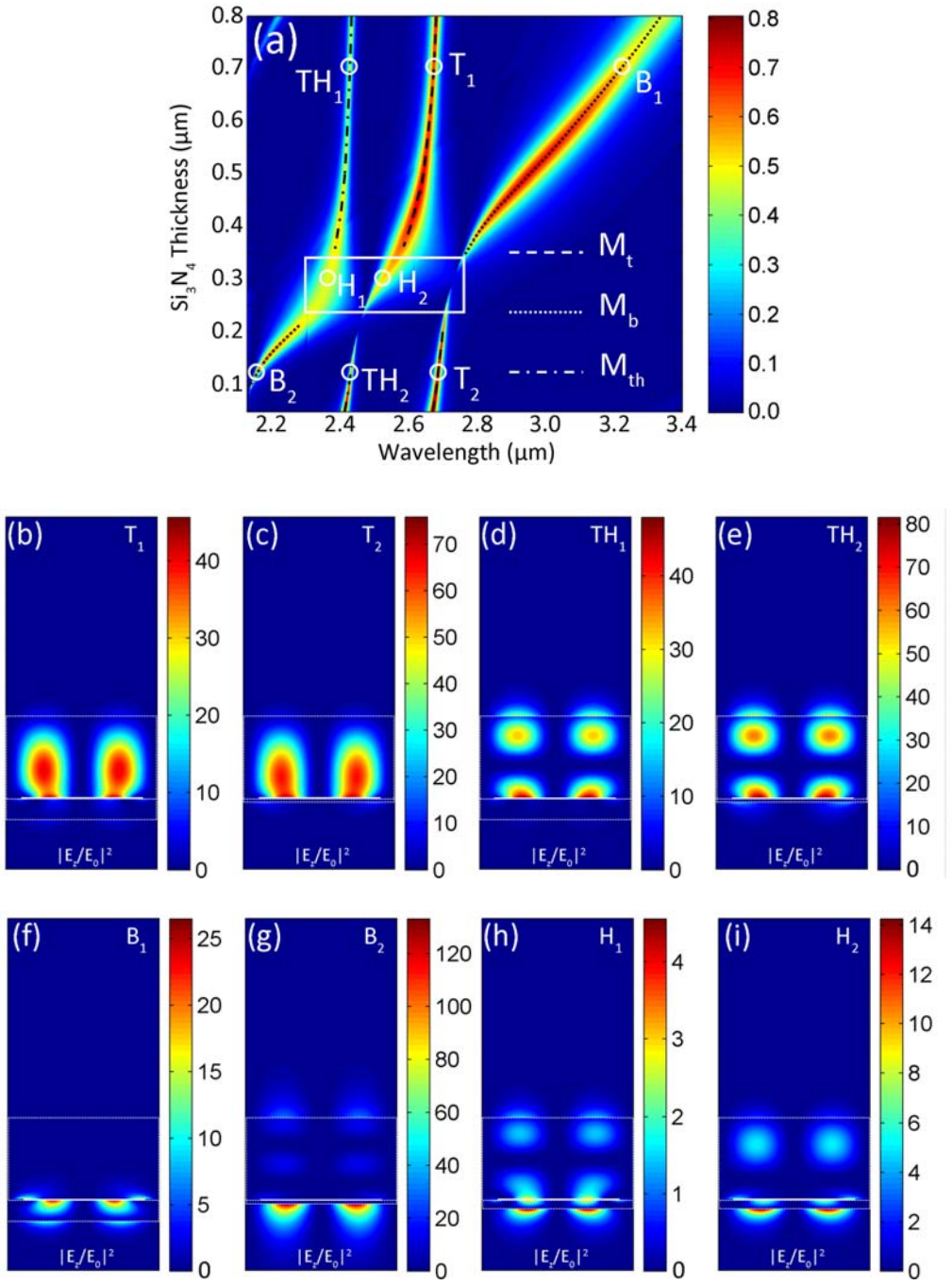

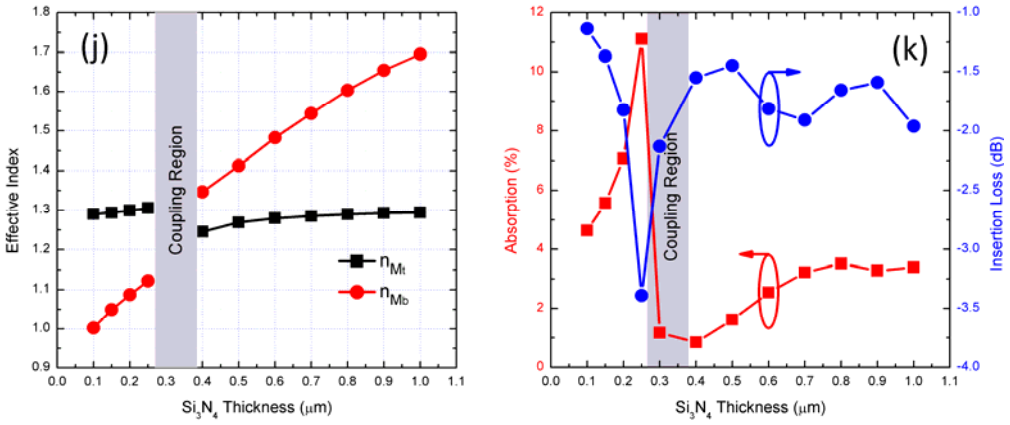

Figure 5.2. (a) Transmission spectra as functions of Si_3N_4 thickness with all other parameters fixed: P = 2.08 μm, G = 250 nm, T = 40 nm and H = 2.7 μm. M_t (dash line), M_b (dot line) and M_{th} (dash dot line) represent the SPP mode at the top Au/MOF/air interface, the SPP mode at the bottom Au/Si_3N_4/air interface, higher order SPP mode at Au/MOF/air interface, respectively. The white rectangular represents the coupling region. The color bar represents the transmission intensity. (b-i) The intensity of the electric field distribution of the representative points shown in (a). (j) Calculated effective RI of the mode of M_t and M_b. (k) Insertion loss (transmission) and absorption as a function of the Si_3N_4 thickness. The gray region is the coupling region.

As shown in Figure 5.2(a), there are three distinct modes in the interested wavelength range: the SPP mode at the top Au/MOF/air interface (M_t, dash line), the SPP mode at the bottom Au/Si_3N_4/air interface (M_b, dot line) and the top SPP (M_{th}, dash dot line) which hybrids with the high order MOF waveguide mode. The

SPP mode M_t always locates around 2.7 μm with small deviation, which results in an effective RI with little change. The intensity of the electric field distribution in Figure 5.2(b) and 5.2(c) clearly verified that the SPP modes are majorly localized within the MOF layer. At slightly shorter wavelength range, the top SPP mode hybrids with higher order waveguide mode of the MOF layer, which is marked as M_{th} in Figure 5.2(a). Figure 5.2(d) and 5.2(e) represent the electric field intensity of M_{th} with a thick (TH_1) and thin (TH_2) Si_3N_4 membrane, which shows little difference in effective RI. For the SPP mode M_b, when the Si_3N_4 thickness is above 400 nm, it appears at longer wavelength compared to M_t because Si_3N_4 (1.960) has a higher RI than that of MOF (1.326). When the Si_3N_4 thickness is less than 250 nm, the mode M_b moves to much shorter wavelength range. This is because the effective RI of the bottom SPP is strongly influenced by the thickness of the Si_3N_4 membrane. The intensity of the electric field distribution in Figure 2(f) and 2(g) indicates the transition from a thick membrane to a thin membrane. When the Si_3N_4 thickness is between 250 ~ 400 nm, however, the effective RI of the top SPP M_t and the bottom SPP M_b are so close to each that strongly coupled modes are formed. In Figure 5.2(a), the region enclosed by the white rectangle represents the coupled mode region, where M_t and M_b cross each other. Within the rectangular region, H_1 represent the coupled mode between M_{th} and M_b, while H_2 represents the coupled mode between M_t and M_b. Clearly, the coupled modes have much lower Q-factors and the electric field intensity is very weak as shown in Figure 5.2(h) and 5.2(i).

We calculate the effective RI as a function of the thickness of Si_3N_4 membrane, which is shown in Figure 5.2(j). In the coupled mode region, however, the Q-factors are low and there are no distinct transmission peaks. Therefore, the effect indices of the coupled modes are not defined. To verify the effect of SEIRA of the suspended nanostructure, an absorption coefficient $k = 1.315\times10^{-4}$ is added into the imaginary part of the RI in the MOF layer to mimic the absorption of CO_2. The value of the imaginary part is calculated from HITRAN database. The total IR absorption and optical transmission at 2.7 μm wavelength as a function of the Si3N4 thickness is shown in Figure 5.2(k). The largest IR absorption appears when the Si_3N_4 thickness is around 250 nm, which is close to the edge of the coupled mode region. If the Si_3N_4 membrane becomes thinner, the IR absorption will actually decrease. This conclusion is different than Au-NPAs on thick substrates, where low RI will lead to higher plasmonic field enhancement in analogy that thinner Si_3N_4 membrane will decrease the effective RI of the bottom substrate. However, the insertion loss at this Si_3N_4 thickness is -3.4 dB, which is too high. From the engineering point of view, sufficient transmission intensity and mechanical support are also needed. If the Si_3N_4 membrane becomes thicker, the IR absorption will first slightly increase due to the Q-factor increase. Then it will stabilize at a relative low IR absorption. This is induced by the higher effective RI of Si_3N_4, where more field tends to locate. Thus, the optimized value is chosen as the cross point of the transmission and absorption curve, which is d = 200 nm. Within the hybrid region, due to the low Q-factor, the absorption is very small.

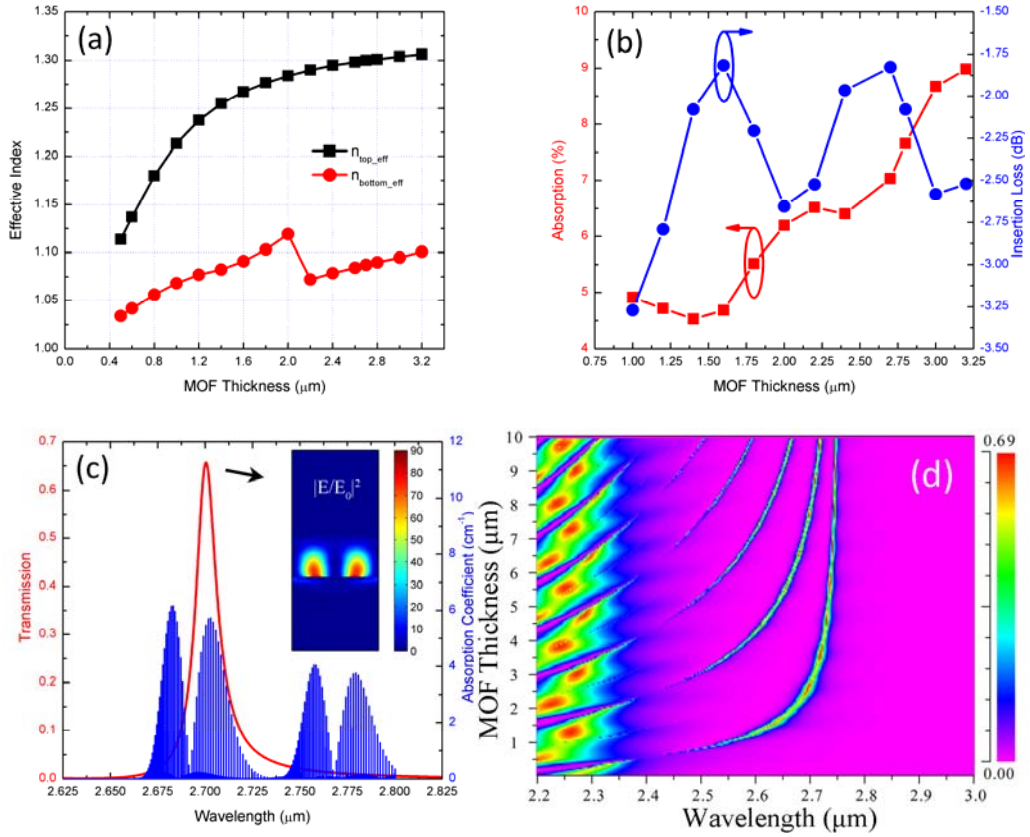

Figure 5.3. (a) Calculated effective RI of mode M_t and M_b. (b) Insertion loss (transmission) and enhanced absorption as a function of MOF thickness. (c) The simulated transmission spectrum (overlapped with CO_2 absorption band). The inset is the electric field distribution at the peak wavelength. (d) The scanning of MOF thickness.

The thickness of the top MOF layer is another critical parameter. Thicker MOF means more adsorption of gas molecules and longer path of IR absorption. However, if the MOF layer is too thick, more higher order modes in MOF layer will show up (Figure 5.3(d)), which are sensitive to the angle deviation of the

incident light and device size[162, 163]. When the incident light is not perfect collimated or the device size is too small, the Q-factor of modes will become much lower, which will reduce the field enhancement. Therefore, an optimized thickness is studied by scanning the MOF thickness while other parameters fixed. As shown in Figure 5.3(a), since the Si_3N_4 thickness d is fixed as 200 nm, the effective RI of mode Mb is always smaller than mode M_t. As the MOF thickness H reduces, the effective RI of M_t becomes closer to air. When the MOF layer becomes thinner than 500 nm, mode M_t will be cutoff. Notably, there is a sudden change around H = 2.0 μm. It is possibly induced by the cavity effect of MOF layer. Similarly, an imaginary part of the RI is added to MOF layer to mimic the CO_2. The absorption as a function of the MOF thickness is shown in Figure 5.3(b). Since the thickness of MOF layer is the absorption path length, thicker MOF layer will result higher absorption. Considering the transmission intensity, the highest point happens at around H = 1.6 μm. As mentioned before, if the adsorption effect of MOF is considered, thicker MOF layer is preferred. However, thicker MOF layer means longer growth time and also possibly difficult for gas molecules to diffuse into MOF. Therefore, after considering all these factors, the optimized MOF thickness is chosen as H = 2.7 μm, which has similar transmission intensity as H = 1.6 μm, and meanwhile all the electric field is still confined inside the MOF layer. After comprehensive study of all the parameters, the final parameters are chosen to be P = 2.08 μm, G = 250 nm, H = 2.7 μm, T = 40 nm and d = 200 nm. The transmission

spectrum of final design, as well as the theoretical CO_2 absorption spectrum is shown in Figure 5.2(c). The inset is the electric field distribution at the peak.

5.2. Experimental Demonstration

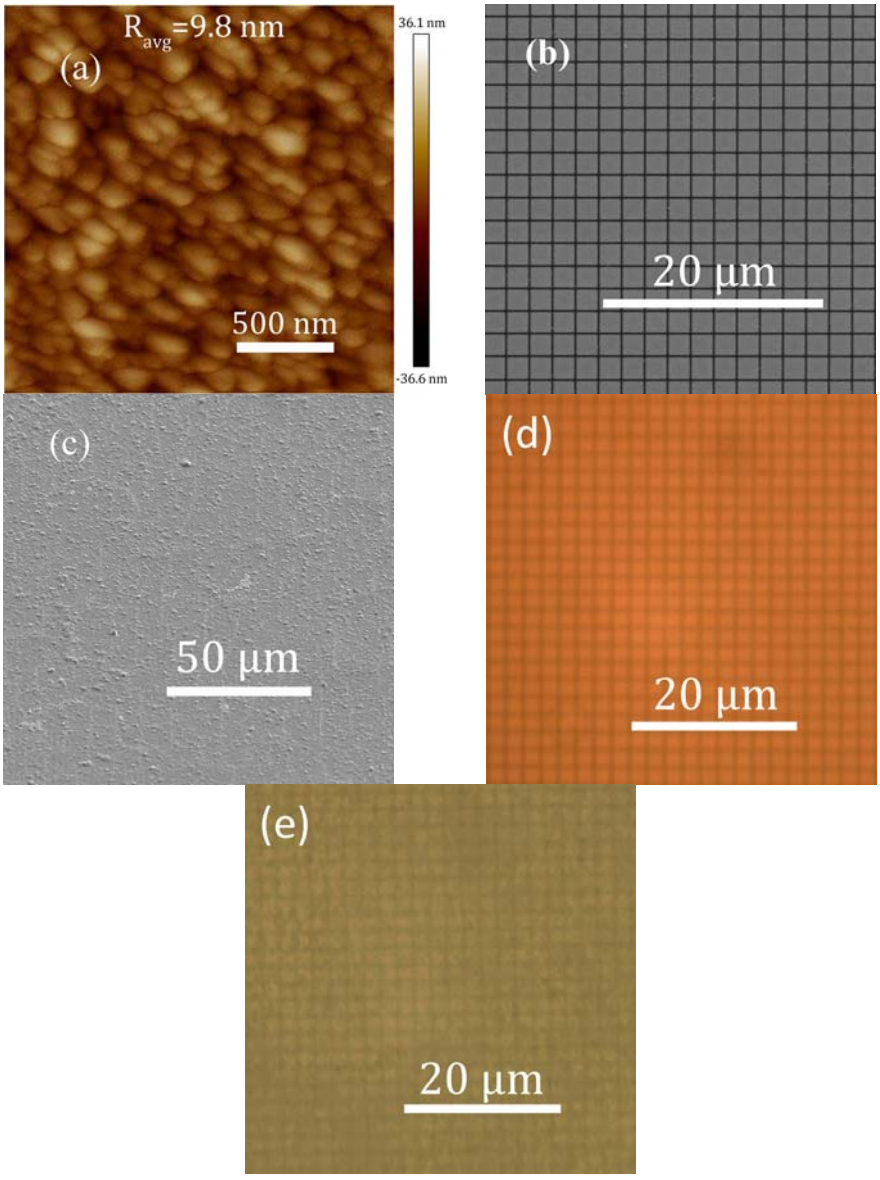

Figure 4. (a) AFM image of ZIF-8 thin film. SEM image of Au-NPA (b) before and (c) after coating MOF. The optical images of Au-NPA (d) before and (e) after coating MOF.

The MOF used in this device is ZIF-8 (zeolitic imidazolate frameworks), which has been extensively investigated due to its excellent thermal stability and selectivity toward CO_2[164]. Since the surface roughness is relative small for ZIF-8, it is suitable for the application in thin film devices. This is demonstrated by the atomic force microscopy (AFM) shown in Figure 5.4(a), which shows a 9.8 nm roughness. Besides, due to the surface property, water molecules can only be adsorbed on the outer surface of ZIF-8 MOF, while CO_2 can diffuse into the inner pores. This hydrophobic surface makes ZIF-8 even more attractive for field sensing application[156]. The ZIF-8 MOF was also characterized by ellipsometry to determine the bulk RI. The Au-NPA is fabricated by focused ion beam (FIB) etching. The scanning electron microscope (SEM) images and optical images of the fabricated Au-NPA before and after coating MOF are shown in Figure 5.4(b-c) and Figure 5.4(d-e). As shown, the MOF layer fully covers the Au-NPA.

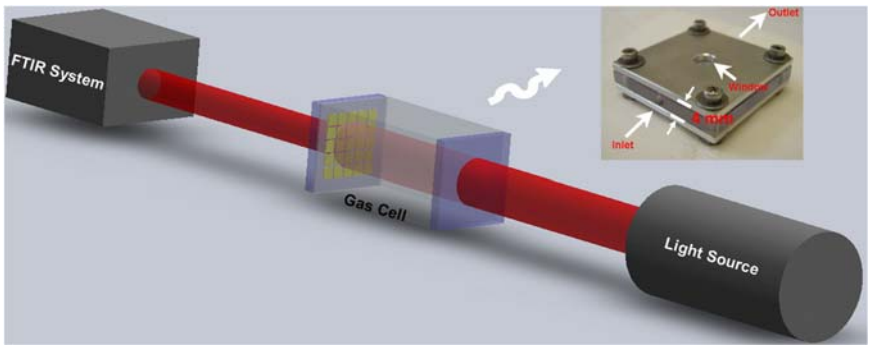

Figure 5.5. The schematic of testing system with home-made gas cell.

To demonstrate the functionality of the device and the enhancement provided by the hybrid plasmonic-MOF device, a quantitative CO_2 absorption measurement was performed by a commercial Fourier transform infrared (FTIR) spectrometer. A home-made gas cell was used in the test, which has 4 mm path length, as shown in Figure 5.5. One side of the gas cell is sealed by a sapphire window and the other side is sealed by the device. Different CO_2 concentrations are obtained by mixing with nitrogen (N_2) using two mass flow controllers (MFCs). The experimentally obtained transmission spectrum is shown Figure 5.6(a), which is broader than the simulation result. The main reason of this broadening effect is the angle deviation of the incident light. Small incident angle will cause spectrum shift and split as shown in Figure 5.6(b). Since the light source of the commercial FTIR is not well collimated, the transmission spectrum will be an integration of all spectra corresponding to different incident angles. To determine the enhancement of the device, the absorption spectra of different CO_2 concentration were collected as shown in Figure 5.6(c). The contribution of MOF and plasmonic effect was determined by two reference samples: both sides of the gas cell sealed by sapphire window; only MOF coated suspended substrate. The absorption spectra of the two references are shown in Figure 5.6(d) and 5.6(e).

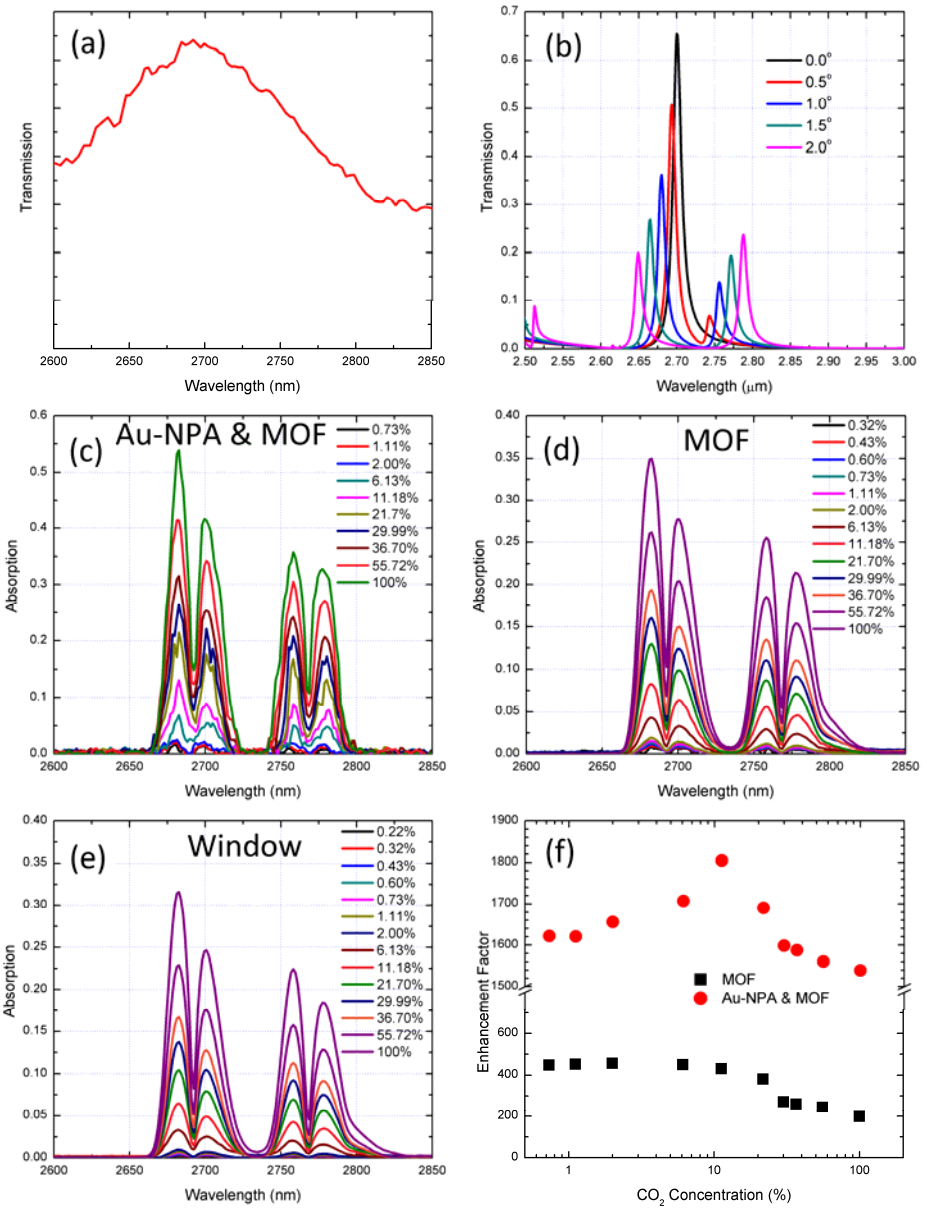
(a)
Transmission
Wavelength (nm)
(b)
0.0°
0.5°
1.0°
1.5°
2.0°
Transmission
Wavelength (μm)
(c) Au-NPA & MOF
0.73%
1.11%
2.00%
6.13%
11.18%
21.7%
29.99%
36.70%
55.72%
100%
Absorption
Wavelength (nm)
(d) MOF
0.32%
0.43%
0.60%
0.73%
1.11%
2.00%
6.13%
11.18%
21.70%
29.99%
36.70%
55.72%
100%
Absorption
Wavelength (nm)
(e) Window
0.22%
0.32%
0.43%
0.60%
0.73%
1.11%
2.00%
6.13%
11.18%
21.70%
29.99%
36.70%
55.72%
100%
Absorption
Wavelength (nm)
(f)
MOF
Au-NPA & MOF
Enhancement Factor
CO2 Concentration (%)

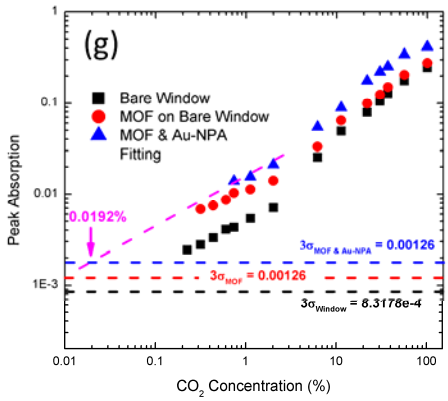

Figure 5.6. (a) The experimental transmission spectrum. (b) The effect of incident angle deviation. The absorption spectra of (c) Au-NPA coated with MOF, (d) bare window and (e) MOF on bare window with different CO_2 concentration. (f) The calculated enhancement factor as a function of CO_2 concentration. (g) The noise analysis of the three devices.

Considering the bare sapphire window reference, since there is no enhancement, the absorption is purely from CO_2 in the gas cell. The absorption coefficient α of CO_2 calculated from this reference will be the actual value under the experimental conditions. For the other reference, due to the presence of MOF, more CO_2 molecules were adsorbed inside the MOF layer, which essentially increases the local absorption coefficient. For the integrated device, in addition to the effect of MOF, the adsorbed CO_2 molecules also interacted with the hybrid field of SPP mode M_t and waveguide mode in MOF, which provides extra enhancement. By comparing the device with the two references, the enhancement factors (EFs) of the device and the contribution of MOF were calculated as shown in Figure 5.6(f).

Noticeably, the major contribution is provided by MOF. The enhancement from plasmonic field is smaller than the simulation, which is caused by the lowered Q-factor. As mentioned before, the broadening is mainly caused by the incident angle deviation. Thus, the EF from plasmonic field can be dramatically improved by using a well collimated light source. Moreover, due to the huge mismatch between the light spot size of the commercial FTIR spectrometer (~ 7 mm in diameter) and the device size (1 mm^2), the power collected by the detector is relative low, which limit the lowest detectable CO_2 concentration in the experiment. However, detection limit can be estimated by analyzing the noise of system. The noise mainly comes from the fluctuation of light source and the dark current noise of the detector. When the transmission intensity is strong enough, the signal will be much higher than the dark noise level. In this case, the major noise will be the fluctuation of the light source. But when the transmission intensity is too weak and the signal is just slightly higher dark noise, the two noise sources will both affect the signal, which is our case. The noise levels (3 times of standard deviation) of the two references and the device are shown in Figure 5.6(g). Since the absolute transmission intensity for the two references is far above the noise level of the detector, the noise will mainly come from light source fluctuation. Therefore, the noise level of three samples are: bare window < MOF on bare window < device. To estimate the detection limit, the Beer-Lambert Law is simplified for low CO_2 concentration situation: $I \approx I_0(1-\alpha \bullet L)$, which means the absorption is linearly proportional to CO_2 concentration. Thus, the cross point of the linear fitting line of the absorption data

at low concentration with the noise level will be the estimated detection limit. As shown in Figure 5.6 (g), the purple dash line represents fitting line and the cross point is labeled by the arrow, which represents the estimated detection limit about 0.0192% (192 ppm). This value can be improved by using a light source with spot size comparable to the device size.

5.3. Summary

In this chapter, we present a suspended Si_3N_4 nano-membrane device integrating plasmonic nano-patch antennas with MOF, which can efficiently adsorb CO_2 through its nanoporous structure. Comparing to the conventional SEIRA sensing relying on localized hot-spots of plasmonic nanostructures, this device engineered the coupled surface plasmon polaritons in the metal-Si_3N_4 and metal-MOF interfaces to achieve strong optical field enhancement across the entire MOF film. We successfully demonstrated on-chip gas sensing of CO_2 with more than 1,800× enhancement factors within a 2.7 μm thin film.

CHAPTER 6. ON-CHIP GAS SPECTROSCOPY USING HIGH RESOLUTION PLASMONIC FILTER ARRAY

In the previous chapters, we demonstrated the possibility of on-chip gas sensing by integrating MOF with plamonic nanostructures. However, in an infrared spectroscopy system, besides the sensor part, wavelength dispersion component is also very critical. In order to realize whole miniaturized device for future field sensing, in this chapter, we present an ultra-compact, cost-effective on-chip near-infrared spectroscopy system for CO_2 sensing using narrow-band optical filter array based on plasmonic gratings with a waveguide layer. By varying the periodicity of the gratings, the transmission spectra of the filters can be continuously tuned to cover the 2.0 μm sensing window with high spectral resolution around 10 nm. Our experimental results show that the on-chip spectroscopy system can successfully resolve the two symmetric vibrational bands of CO_2 at 2.0 μm wavelength, which proves its potential to replace the expensive commercial IR spectroscopy system for on-site gas sensing.

6.1. Overview of On-Chip Spectroscopy System

Optical spectroscopy is a key technology for the detection of a wide variety of atoms and molecules in different applications, such as chemistry, biology and environmental sciences. As compared to many other types of sensing technologies, spectroscopic techniques have the advantage of high selectivity from the "fingerprint" of the spectrum. Absorption spectroscopy, fluorescence spectroscopy

and Raman spectroscopy all provide complementary information about the identity and concentration of the molecules. Despite the advantages spectroscopic techniques, most commercially available IR spectroscopy systems, such as FTIR spectroscopy[165] and TDLS[166], are expensive bulky desktop instruments, which is not suitable for field sensing. If the key parts of the spectroscopy system could be integrated on a small chip, the system will be dramatically miniaturized and cost-effective, with the potential of massive parallelism and multiplexing. Therefore, the effort for developing low cost portable IR spectroscopy system is continuously growing.

Several on-chip spectroscopy methods have been reported to realize high resolution based on different configurations, such as arrayed waveguide grating (AWG)[167], Echelle diffraction grating (EDG)[168], superprism-based photonic crystal[169], microresonator array[170], filter array based on Fabry-Perot (FP) cavity[171] and so on. However, these techniques suffer from the tradeoff between spectrum resolution and operating bandwidth, as well as complicated fabrication process, which limits their practice applications. In addition to these techniques, optical filter based on surface plasmon resonance is also very promising, due to their high tunability and simple fabrication. Plasmonic filters composed of metal film with subwavelength-size periodic hole arrays or slot arrays act as optical filters owing to the interference of SPPs between adjacent holes or slots, which is also referred as extraordinary transmission (EOT). The transmission properties of plasmonic filters are mainly defined by their physical structure. This means that by

simply changing the size, shape, and separation of the hole or slot, the transmission spectra can be easily controlled. Owing to this feature, plasmonic filters are very cost competitive. Furthermore, due to the fabrication process of plasmonic filters, they can be easily integrated with CMOS technologies.

6.1.1. Extraordinary Transmission

EOT was first discovered by Ebbesen in 1998[161]. In the experiment, a broadband light was incident on a periodic silver hole array, whose diameter was 1/10 of the wavelength. A strong transmission peak was observed which was several orders higher than the value predicted by the classic diffraction theory. According to the classic diffraction theory[172], the transmission is proportional to the forth order of the hole's radius

$$T \approx \frac{64}{27\pi^2}\left(\frac{r}{\lambda}\right)^4 \tag{6.1}$$

where λ is the wavelength of the incoming light, being r the radius of the hole. This enhanced abnormal transmission peak is the origin of the name of EOT.

The commonly accepted theory of EOT is the coupling between SPPs and the incident light[173]. When the momentum matching condition between incident light and SPPS is met, traveling SPPs or localized SPPs will be created which will bind the energy of optical field into one side of the metal surface with the help of the periodic hole or slot array. The trapped energy will spread to the other side of the metal film and then radiates out. When the metal film is thin enough, the coupling between the SPPs on both side of the metal film will lead to resonance

mode, resulting in an enhanced transmission at specific wavelength. Studies also revealed that the transmission spectrum is determined by the metal material and the structure parameters of the hole or slot array, such as period, the shape and size of the holes, the thickness of metal film and the medium adjacent to the metal film.

By applying the momentum-matching conditions, the peak positions λ_{max} at normal incidence for a two-dimensional array can be approximately determined. For a hole with square array, the λ_{max} of the transmission spectrum can be estimated by the following equation

$$\lambda_{max} = \frac{P}{\sqrt{i^2+j^2}} \sqrt{\frac{\varepsilon_m \varepsilon_d}{\varepsilon_m+\varepsilon_d}} \tag{6.2}$$

where integers i and j are the resonance mode along x axis and y axis respectively, ε_m and ε_d are the dielectric constant of metal and surrounding medium respectively, and P is the period of the array. For a triangular array, the λ_{max} is determined by

$$\lambda_{max} = \frac{P}{\sqrt{\frac{4}{3}(i^2+ij+j^2)}} \sqrt{\frac{\varepsilon_m \varepsilon_d}{\varepsilon_m+\varepsilon_d}} \tag{6.3}$$

For structure with different periods in x and y axes, the λ_{max} can be estimated by

$$\lambda_{max} = \frac{ab}{\sqrt{i^2b^2+j^2a^2}} \sqrt{\frac{\varepsilon_m \varepsilon_d}{\varepsilon_m+\varepsilon_d}} \tag{6.4}$$

where integers a and b are the period in x axis and y axis respectively.

Although EOT is very attractive for optical filter application, the transmission spectra of the EOT devices are typically too broad for spectroscopy. Thus, they are

mainly used as color filters. In this chapter, we propose a new design to achieve narrow transmission peak by coupling the EOT with waveguide mode.

6.2. Theoretical Study

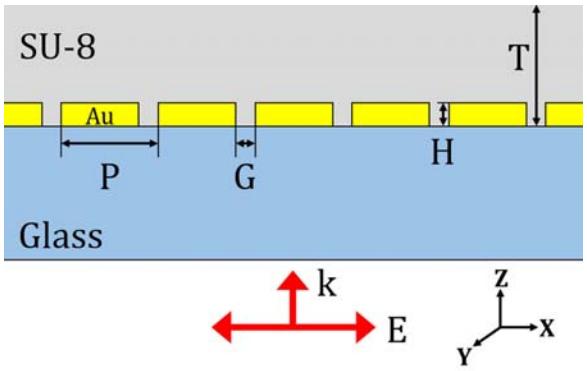

Figure 6.1. The configuration of the plasmonic filter.

The configuration of the plasmonic filter is shown in Figure 6.1, which consists of a gold (Au) thin film with periodic nano-slits on a quartz (n_{sub}=1.45) substrate. A layer of UV cured SU-8 (n_{SU-8}=1.57) photoresist covers the Au thin film, serving as a waveguide layer. Transverse magnetic (TM) polarized light will be launched from the substrate side and normally incident on the filters. By varying the period P of the nano-slit, the transmission peak can be continuously tuned. The periodicity P also slightly affects the peak transmission intensity. However, within our interested wavelength range (1.98 ~ 2.04 μm), the effect is minor.

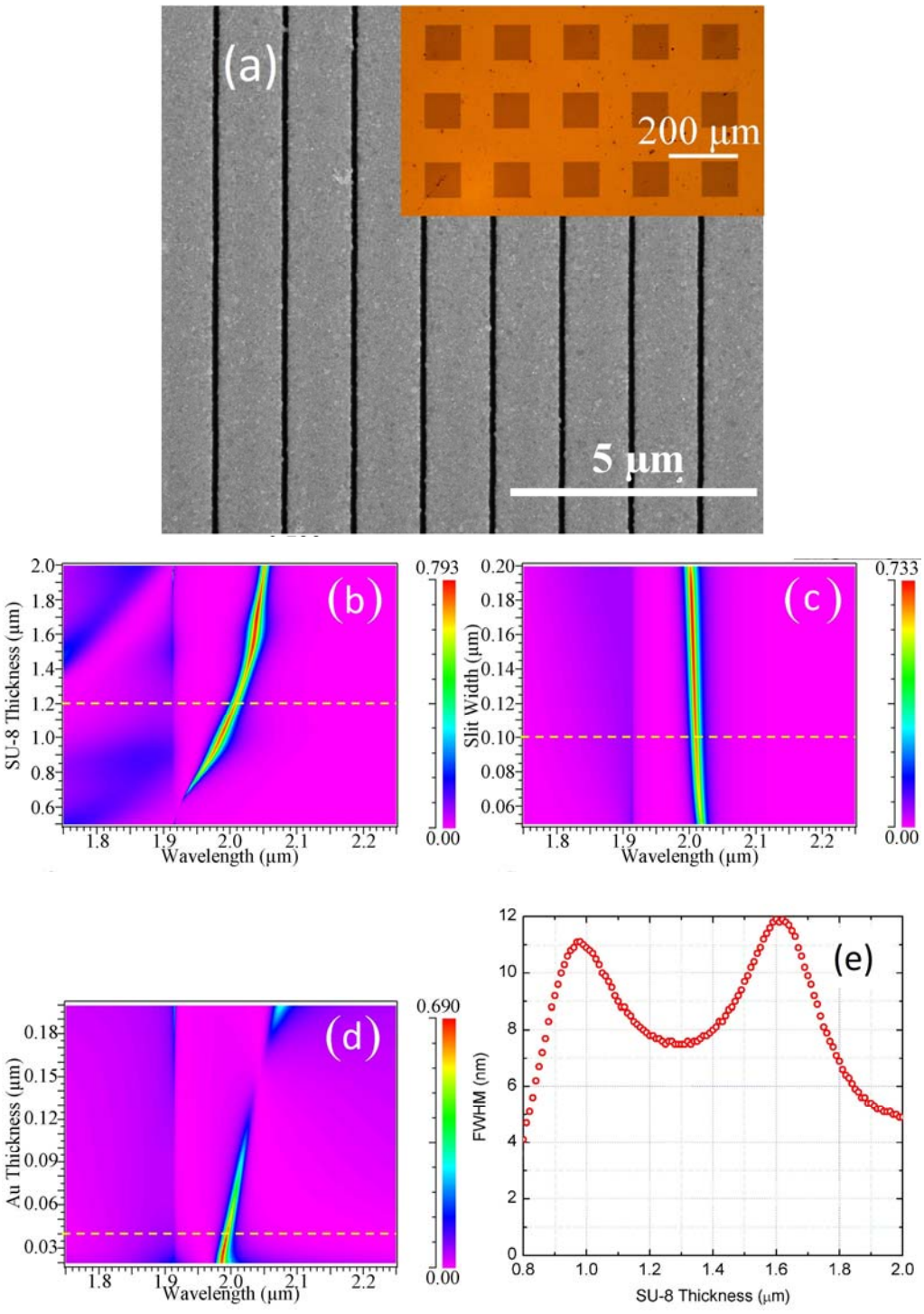
(a)
200 μm
5 μm
(b)
SU-8 Thickness (μm)
Wavelength (μm)
0.793
0.00
(c)
Slit Width (μm)
Wavelength (μm)
0.733
0.00
(d)
Au Thickness (μm)
Wavelength (μm)
0.690
0.00
(e)
FWHM (nm)
SU-8 Thickness (μm)

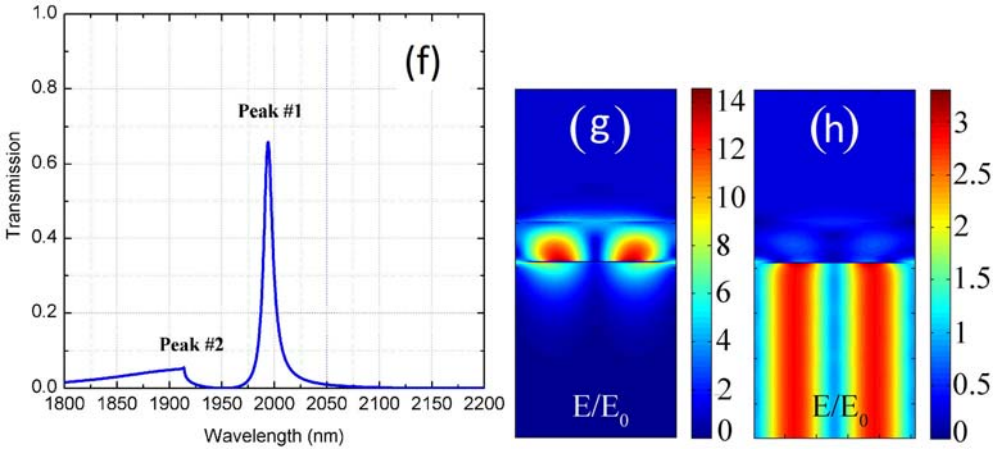

Figure 6.2. (a) Scanning electron microscope image of Au film with nano-slit. Inset is the optical image of the filter array. Transmission spectra of the plasmonic filter: (b) the effect of SU-8 thickness, (c) slit width and (d) Au film thickness. (e) The full width half maximum (FWHM) of the transmission spectrum as a function of SU-8 thickness. (f) An example of the transmission spectrum using the optimized parameters. (g) Hybrid electric field distribution of major peak and (h) side-band. The electric filed amplitude is normalized to that of the incident light E_0. Dash lines represent the design parameters used in the experiment.

The scanning electron microscope (SEM) image of the Au film with nano-slit is shown in Figure 6.2(a). There are three parameters that affect the transmission spectrum: the slit width G, Au thin thickness H and SU-8 thickness T, which are scanned to achieve small full width half maximum (FWHM), high transmission amplitude and less side-bands effects based on rigorous coupled-wave analysis (RCWA). As shown in Figure 6.2(b-d), the effects of the SU-8 thickness, slit width

and Au film thickness to the transmission spectrum are studied. It is found that the thickness of SU-8 plays the most important role. It not only influences the FWHM, but also contributes to the transmission amplitude and side-bands. Thinner SU-8 layer may cause cut-off (discontinuity) of the waveguide mode, while thicker film will generate higher order waveguide modes and the coupling between higher order waveguide modes and Rayleigh Anomaly (RA). RA is associated with light diffracted parallel to the grating surface, which is determined by dielectric constant of the substrate, surrounding medium and the grating pitch[155]. In our case, the RA happens on the substrate side. The FWHM of the spectrum as a function is shown in Figure 6.2(e). For the slit width, it only slightly affects the transmission amplitude and FWHM. Wider slit width will allow more light passing through, but the FWHM will also increase. For Au film thickness, thinner film shows larger transmission amplitude and larger FWHM. However, if the Au thickness is too thin, the overall noise level of the spectrum will increase. Besides, at certain thickness, the cavity resonance in the nano-slit and the surface plasmon polariton on Au surface will have deconstructive interference, which will cause the discontinuity shown in the Figure 6.2(d)[174-178]. Finally, the three parameters are chosen to be G = 100 nm, H = 40 nm and T = 1.2 μm (dash line). Although the FWHM at T = 1.2 μm is slightly larger than that at T = 1.3 μm (< 1 nm), the side-band effect is less at T = 1.2 μm. An example of the transmission spectrum using the chosen values is shown in Figure 6.2(f). There are two transmission peaks on the spectrum, representing two different modes. The major peak (#1) at ~2.0 μm represents the

coupling mode between surface plasmon at SU-8/Au interface and the narrow-band waveguide mode supported by the SU-8 waveguide layer. The side band (#2) at ~ 1.91 μm is due to the Rayleigh Anomaly in the glass substrate[162, 179-182]. The normalized electric field amplitude distribution of the two modes is shown in Figure 6.2(g) and 6.2(h).

6.3. Experimental Demonstration

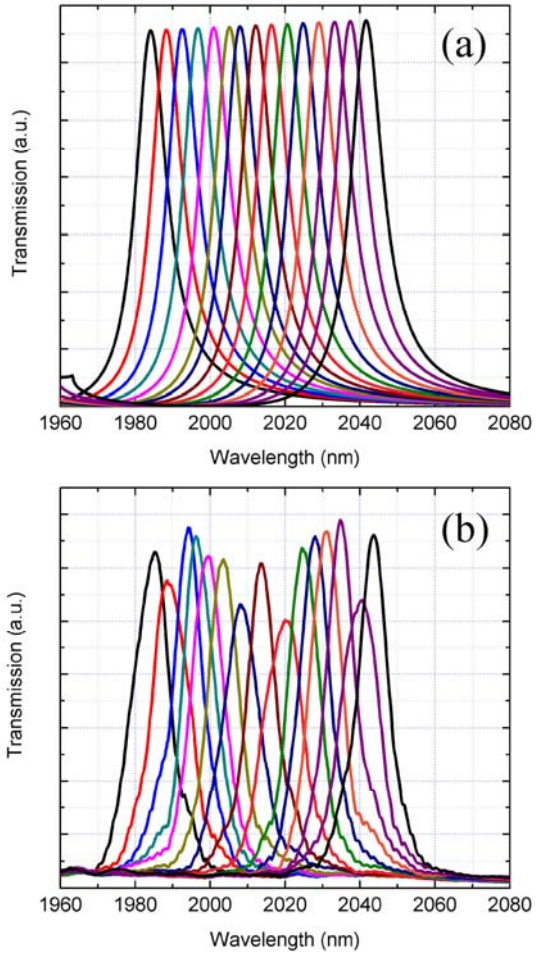

Figure 6.3. (a) Numerically simulated and (b) experimentally obtained transmission spectrum of each filter. G = 100 nm, H = 40 nm, T = 1.2 μm and the period varies from 1313nm to 1354nm with 4 nm step.

The filters are fabricated by focused ion beam (FIB) etching followed spin-coating SU-8. As shown in the inset of Figure 6.3(b), eventually, there are 15 filters in total. The size of each filter is 100 μm × 100 μm and the total area of the filter array is less than 1 mm^2. The transmission spectrum of each filter is calibrated by an optical spectrum analyzer (OSA). Figure 6.3(a) and 6.3(b) show both the numerically simulated and experimentally obtained transmission spectrum of each filter. Comparing the two sets of spectra, two discrepancies between simulation and experiment: (1) the amplitude of the transmission spectra in the experiment fluctuate from filter to filter. It is mainly due to the non-uniformity of the SU-8 film. (2) The FWHM of the experimental obtained spectrum (10 ~ 12 nm) is slightly larger than the simulation (7 ~ 9 nm), which is induced by the variation of both the nano-silt width and imperfection of the thermal evaporated Au thin film.

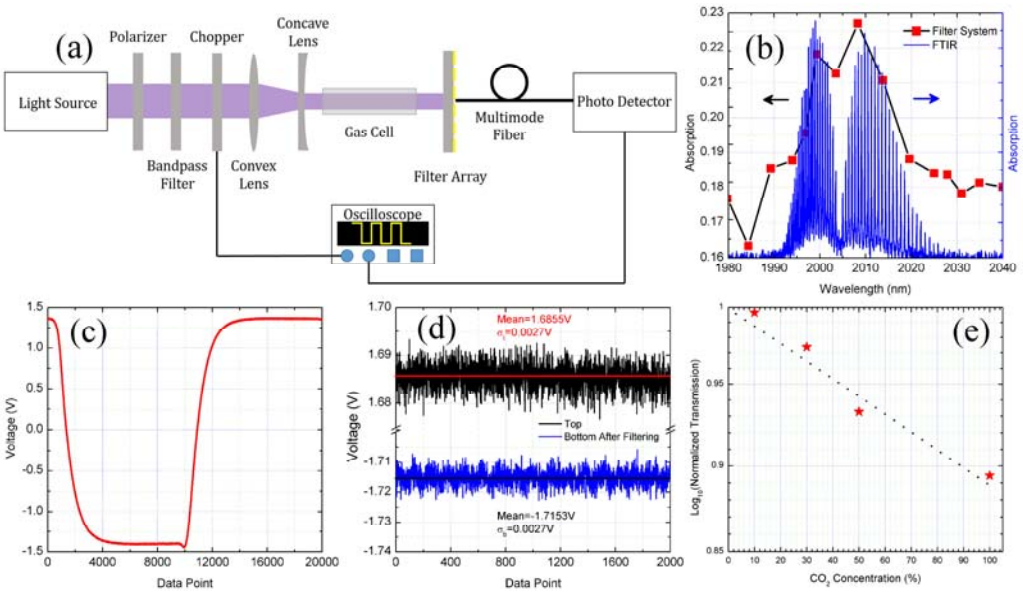

Figure 6.4. (a) Experiment setup for CO_2 sensing; (b) experimental absorption spectrum of CO_2; (c) Signal received by oscilloscope; (d) noise level of the top and bottom flat region after filtering. (e) Normalized transmission as a function of CO_2 concentration.

To demonstrate the capability of the filter array for gas sensing application, a spectroscopy system using the filter array is built as shown in Figure 6.4(a). The collimated light from a supercontinuum light source (NKT Photonics, 400 nm ~ 2400 nm, 10 kHz) first passes through a linear polarizer (Thorlabs Inc., LPNIR050) to obtain TM light. A bandpass filter (Thorlabs Inc., FB2000-500) is used to shrink the wavelength range to 1750 nm to 2250 nm to avoid undesired side bands. Due to the large beam diameter of the light source comparing to the filter, a simple beam expander is reversely used to shrink the beam size to obtain high power density.

The shrunk light passes then through a 10 cm quartz gas cell. The light transmitted through the filter is collected by a multi-mode fiber (MMF) and delivered to a PbS photodetector (Thorlabs, Inc., PDA30G). Since the photodetector is AC coupled, a chopper is applied to convert the CW light to pulsed light. Finally, the electric signal from the photodetector is sent to an oscilloscope. It should be noted that, although in the experiment setup, an MMF is used to collect the light transmitted through the filters, it can be replaced by a charge-coupled device (CCD) or photodetector array placed directly behind the filter array. In this way, signals from each filter can be collected simultaneously, which allows high speed detection. Moreover, without MMF, there will be no alignment or coupling stability issue, which may induce extra noise.

The transmitted power of each filter through a gas cell filled with CO_2 is recorded. The same measurement for Ar is taken as the reference. Since Ar does not absorb any light around 2.0 μm, the subtraction between the transmitted power of CO_2 and Ar will be the NIR absorption due to CO_2. The absorption spectrum of CO_2 obtained by this system (black line with red square) is shown in Figure 6.4(b). As a comparison, the experimental data from conventional FTIR (blue lines) is also shown. It is clearly seen that the two vibration bands are resolved, which matches the experimental results using conventional FTIR. The slight variation (~1nm) between these two experimental methods can possibly come from fabrication variation and the limited resolution of the filter array.

To evaluate the capability of current system, the noise of the signal is studied. After chopping, the signal received by the oscilloscope is a square wave as shown in Figure 6.4(c). The voltage difference between the top and bottom flat regions will represent the actual voltage associated with transmitted light. The top region represents the signal when light is blocked by the chopper, and the bottom region represents the signal when the light is unblocked. It is noticed that, in the bottom region, there is a regular low frequency (~10 kHz) variation in addition to the high frequency noise. This variation is caused by the frequency of the pulsed light source. Such regular variation can be easily filtered out, as shown in Figure 6.4(d). The noises of the top and bottom flat regions are represented by the standard deviation σ_t and σ_b, both of which are 0.0027V. When there is absorption caused by CO_2, the bottom trace will move up. In order to distinguish the signal change due to the CO2 absorption, the voltage change has to be at least $3\sigma_t + 3\sigma_b$[183, 184]. Therefore, the minimum detection is defined to be $\sigma = 3\sigma_t + 3\sigma_b$. The voltage change at the peak absorption is 0.7537 V, which is about 46.52 times of σ. We measured the normalized transmission as a function of different CO_2 concentration, which is shown in Figure 6.4(e). A good linearity is observed, which matches the law of Beer-Lambert absorption. Here, we also define the sensitivity to be minimum detectable CO_2 concentration × optical absorption length. Therefore, for our current system, the sensitivity is about 214,957 ppm·cm. Michael E. Webber et al.[185] reported 144,000 ppm·cm sensitivity for vent gas in a bioreactor and 5,000 ppm·cm[186] for combustion gas using distributed feedback laser. It should be

noted that as the noise level is relatively constant, the voltage change due to the CO_2 absorption is proportional to the intensity of the input light. Higher input light intensity will achieve lower detection limit. Therefore, the sensitivity of our on-chip NIR spectroscopy system can be improved by increasing the input light intensity or using a more stable light source. A lock-in amplifier to detect only the chopping frequency can also improve the signal-to-noise ratio and hence improve the detection limit.

6.4. Summary

In summary, we have designed and experimentally demonstrated an NIR on-chip spectroscopy system for CO_2 by an array of narrow-band plasmonic filters with 10 ~ 12 nm spectral resolution. The two vibrational bands of CO_2 are resolved, which matches the theoretical data from HITRAN database. By evaluating the noise level of the system, the sensitivity of current system is estimated to be 214,957 ppm·cm. The sensitivity can be further improved by suppressing the noise using lock-in amplifiers. Due to the advantage of compactness, low-cost and easy-to-fabricate, this plasmonic filter array shows great potentials to replace the expensive and bulky FTIR spectroscopy system for mobile NIR gas sensing.

CHAPTER 7. CONCLUSIONS

Surface-enhanced infrared absorption (SEIRA) is capable of identifying molecular fingerprints by resonant detection of infrared vibrational modes through the coupling with plasmonic modes of metallic nanostructures. However, SEIRA for on-chip gas sensing is still not very successful due to the intrinsically weak light-matter interaction between photons and gas molecules. This dissertation has dealt with the development of on-chip device by integrating plasmonic nanostructures with nanoporous material to achieve ultra-long absorption length.

The solution we proposed is integrating nanoporous material MOF with periodic plasmonic nanostructures, which can provide two sources of enhancement: (1) high plasmonic field enhancement due to the high Q-factor resonance; (2) preconcentrating effect of MOF. Before the integration, the optical properties of MOF material were characterized in Chapter 2 for future device design. To demonstrate the capability of MOF used for a gas sensor, in Chapter 3, a simple evanescent field based optical fiber gas sensor was experimentally demonstrated by coating MOF onto the partially etched fiber surface. The experimental results show 20 ppm detection limit of CO_2 within only 5 cm sensing length, which prove the high potential for optical sensing application.

Chapter 4 and Chapter 5 discuss the two design of integrating MOF with periodic plasmonic nanostructures for CO_2 detection. Both designs are experimentally demonstrated to have a high enhancement factor due to the coupled

SPPs mode in the entire MOF layer and the preconcentrating effect of MOF. The two designs show a route for future on-chip gas sensing devices based on SEIRA spectroscopy.

For future application of on-chip spectroscopy system, a simple narrow-band plasmonic filter array with 10 ~ 12 nm spectral resolution was designed and demonstrated in Chapter 6. This plasmonic filter array shows great potentials to replace the expensive and bulky FTIR spectroscopy system for portable on-chip gas spectroscopy system.

In summary, our work integrating plasmonic nanostructures with nanoporous material has successfully extend the powerful SEIRA spectroscopy to on-chip gas sensing. The plasmonic enhancement of this devices need to be further improved by using a well collimated infrared light source. The limit of detection requires small light spot size to achieve high signal-to-noise ratio. Such device will need to be improved in the future work by designing a sharp plasmonic resonance peak with low incident angle dependence. The fabrication method also need to be improved to achieve relative larger device to tolerance large spot size of common light source on the market, such as LED.

Reference

[1] G. Korotcenkov, Handbook of Gas Sensor Materials: Properties, Advantages and Shortcomings for Applications Volume 1: Conventional Approaches, Springer New York, 2013.

[2] S.V. Ryabtsev, A.V. Shaposhnick, A.N. Lukin, E.P. Domashevskaya, Sensor Actuat B-Chem, 59 (1999) 26-29.

[3] Y. Sakumura, Y. Koyama, H. Tokutake, T. Hida, K. Sato, T. Itoh, T. Akamatsu, W. Shin, Sensors-Basel, 17 (2017).

[4] X. Chen, F.J. Xu, Y. Wang, Y.F. Pan, D.J. Lu, P. Wang, K.J. Ying, E.G. Chen, W.M. Zhang, Cancer-Am Cancer Soc, 110 (2007) 835-844.

[5] R. Pitarma, G. Marques, B.R. Ferreira, J Med Syst, 41 (2017).

[6] L. 'T Hart, P. Storme, W. Anaf, G. Nuyts, F. Vanmeert, W. Dorrine, K. Janssens, K. de Wael, O. Schalm, Appl Phys a-Mater, 122 (2016).

[7] J.Y. Kim, C.H. Chu, S.M. Shin, Ieee Sens J, 14 (2014).

[8] M. van den Bossche, N.T. Rose, S.F.J. De Wekker, Sensor Actuat B-Chem, 238 (2017) 501-509.

[9] D. Schepers, G. Schulze, W. Frenzel, Anal Chim Acta, 308 (1995) 109-114.

[10] C.N. Hewitt, A.V. Jackson, Handbook of Atmospheric Science: Principles and Applications, Wiley, 2008.

[11] H.L. Zuo, F.Q. Yang, W.H. Huang, Z.N. Xia, J Chromatogr Sci, 51 (2013) 704-715.

[12] A.B. Littlewood, Gas Chromatography: principles, techniques and applications, Academic Press, 1967.

[13] P.T. Moseley, B.C. Tofield, Solid state gas sensors, A. Hilger, 1987.

[14] G.F. Fine, L.M. Cavanagh, A. Afonja, R. Binions, Sensors-Basel, 10 (2010) 5469-5502.

[15] C.X. Wang, L.W. Yin, L.Y. Zhang, D. Xiang, R. Gao, Sensors-Basel, 10 (2010) 2088-2106.

[16] N. Barsan, U. Weimar, J Phys-Condens Mat, 15 (2003) R813-R839.

[17] N. Funazaki, S. Kume, A. Hemmi, S. Ito, Y. Asano, S. Yamashita, Sensor Actuat B-Chem, 13 (1993) 466-469.

[18] W.T. Hung, K.C. Ho, J New Mat Electr Sys, 5 (2002) 305-313.

[19] J. Lee, G. Du Plessis, D.W.M. Arrigan, D.S. Silvester, Anal Methods-Uk, 7 (2015) 7327-7335.

[20] B. Hök, A. Blückert, J. Löfving, Sensor Rev, 20 (2000) 139-142.

[21] J.S. Liu, Y.Y. Lu, Sensors-Basel, 14 (2014) 6844-6853.

[22] S.J. Martin, G.C. Frye, J.J. Spates, M.A. Butler, Gas sensing with acoustic devices, in: 1996 IEEE Ultrasonics Symposium. Proceedings, 1996, pp. 423-434 vol.421.

[23] X. Chong, K.-J. Kim, E. Li, Y. Zhang, P.R. Ohodnicki, C.-H. Chang, A.X. Wang, Sensors and Actuators B: Chemical, 232 (2016) 43-51.

[24] K.J. Kim, X.Y. Chong, P.B. Kreider, G.H. Ma, P.R. Ohodnicki, J.P. Baltrus, A.X. Wang, C.H. Chang, J Mater Chem C, 3 (2015) 2763-2767.

[25] X.Y. Chong, K.J. Kim, P.R. Ohodnicki, E.W. Li, C.H. Chang, A.X. Wang, Ieee Sens J, 15 (2015) 5327-5332.

[26] X. Liu, S.T. Cheng, H. Liu, S. Hu, D.Q. Zhang, H.S. Ning, Sensors-Basel, 12 (2012) 9635-9665.

[27] B. Commoner, D. Lipkin, Science, 110 (1949) 41-43.

[28] L.H. Crawley, Application of Non-dispersive Infrared (NDIR) Spectroscopy to the Measurement of Atmospheric Trace Gases: A Thesis Presented in Partial Fulfilment for the Degree of Master of Science in Environmental Science at the University of Canterbury, Christchurch, New Zealand, University of Canterbury, 2008.

[29] R.P. Lucht, S. Hanna, R. Barron-Jiminez, J.A. Caton, T. Walther, Absorption based UV-sensors for combustion processes, in: SIcon/01. Sensors for Industry Conference. Proceedings of the First ISA/IEEE. Sensors for Industry Conference (Cat. No.01EX459), 2001, pp. 300-302.

[30] G.E. Fodor, S.R.I.S.A.T.T. FUELS, L.R.F. ACILITY., Analysis of Natural Gas by Fourier Transform Infrared Spectroscopy, Defense Technical Information Center, 1996.

[31] M. Lackner, Gas Sensing in Industry by Tunable Diode Laser Spectroscopy (TDLS): Review on State-of-the-art Metrology for Demanding Species Concentration, Temperature and Pressure Measurement Tasks, Verlag ProcessEng Engineering, 2008.

[32] K.H. Michaelian, Photoacoustic IR Spectroscopy: Instrumentation, Applications and Data Analysis, Wiley, 2010.

[33] G. Berden, R. Engeln, Cavity Ring-Down Spectroscopy: Techniques and Applications, Wiley, 2009.

[34] J. Hodgkinson, R.P. Tatam, Meas Sci Technol, 24 (2013).

[35] R. Bogue, Sensor Rev, 35 (2015) 133-140.

[36]https://en.wikipedia.org/w/index.php?title=Fourier_transform_infrared_spectroscopy&oldid=771828870, in.

[37] F.P. Miller, A.F. Vandome, M.B. John, Michelson Interferometer, VDM Publishing, 2010.

[38] P.R. Griffiths, J.A. De Haseth, J.D. Winefordner, Fourier Transform Infrared Spectrometry, Wiley, 2007.

[39] https://www.copac.dk/photoacoustic-spectroscopy/.

[40] http://www.fz-juelich.de/iek/iek-8/EN/Expertise/MeasurementTechniques/TraceGasesRadicals/CacityRingDown/CavityRingDown_node.html.

[41] T. Fukuchi, T. Shiina, Industrial Applications of Laser Remote Sensing, Bentham Science, 2012.

[42] S. Lakkis, R. Younes, Y. Alayli, M. Sawan, Sensor Rev, 34 (2014) 24-35.

[43] J. Homola, S.S. Yee, G. Gauglitz, Sensor Actuat B-Chem, 54 (1999) 3-15.

[44] M. Li, S.K. Cushing, N.Q. Wu, Analyst, 140 (2015) 386-406.

[45] Z.Q. Liang, J. Sun, Y.Y. Jiang, L. Jiang, X.D. Chen, Plasmonics, 9 (2014) 859-866.

[46] M. Bauch, K. Toma, M. Toma, Q.W. Zhang, J. Dostalek, Plasmonics, 9 (2014) 781-799.

[47] Y. Jiang, H.Y. Wang, H. Wang, B.R. Gao, Y.W. Hao, Y. Jin, Q.D. Chen, H.B. Sun, J Phys Chem C, 115 (2011) 12636-12642.

[48] C.X. Niu, Q.W. Song, G. He, N. Na, J. Ouyang, Anal Chem, 88 (2016) 11062-11069.

[49] Y. You, Q.W. Song, L. Wang, C.X. Niu, N. Na, J. Ouyang, Nanoscale, 8 (2016) 18150-18160.

[50] B. Fu, J.D. Flynn, B.P. Isaacoff, D.J. Rowland, J.S. Biteen, J Phys Chem C, 119 (2015) 19350-19358.

[51] A.L. Feng, M.L. You, L.M. Tian, S. Singamaneni, M. Liu, Z.F. Duan, T.J. Lu, F. Xu, M. Lin, Sci Rep-Uk, 5 (2015).

[52] N. Gandra, C. Portz, L.M. Tian, R. Tang, B.G. Xu, S. Achilefu, S. Singamaneni, Angew Chem Int Edit, 53 (2014) 866-870.

[53] R.A. Halvorson, P.J. Vikesland, Environ Sci Technol, 44 (2010) 7749-7755.

[54] D. Cialla, A. Marz, R. Bohme, F. Theil, K. Weber, M. Schmitt, J. Popp, Anal Bioanal Chem, 403 (2012) 27-54.

[55] P.L. Stiles, J.A. Dieringer, N.C. Shah, R.R. Van Duyne, Annu Rev Anal Chem, 1 (2008) 601-626.

[56] A. Tittl, H. Giessen, N. Liu, Nanophotonics-Berlin, 3 (2014) 157-180.

[57] J.M. Bingham, J.N. Anker, L.E. Kreno, R.P. Van Duyne, J Am Chem Soc, 132 (2010) 17358-17359.

[58] D. Buso, G. Busato, M. Guglielmi, A. Martucci, V. Bello, G. Mattei, P. Mazzoldi, M.L. Post, Nanotechnology, 18 (2007) 475505.

[59] N. Liu, F.F. Wen, Y. Zhao, Y.M. Wang, P. Nordlander, N.J. Halas, A. Alu, Nano Lett, 13 (2013) 142-147.

[60] D. Nau, A. Seidel, R.B. Orzekowsky, S.H. Lee, S. Deb, H. Giessen, Opt Lett, 35 (2010) 3150-3152.

[61] M. Ando, T. Kobayashi, S. Iijima, M. Haruta, Sensor Actuat B-Chem, 96 (2003) 589-595.

[62] G. Sirinakis, R. Siddique, I. Manning, P.H. Rogers, M.A. Carpenter, J Phys Chem B, 110 (2006) 13508-13511.

[63] P.R. Ohodnicki, C.J. Wang, S. Natesakhawat, J.P. Baltrus, T.D. Brown, J Appl Phys, 111 (2012).

[64] S. Ahmadnia-Feyzabad, A.A. Khodadadi, M. Vesali-Naseh, Y. Mortazavi, Sensor Actuat B-Chem, 166 (2012) 150-155.

[65] L.I.B. Silva, A.C. Freitas, T.A.P. Rocha-Santos, M.E. Pereira, A.C. Duarte, Talanta, 83 (2011) 1586-1594.

[66] E. Maeda, S. Mikuriya, K. Endo, I. Yamada, A. Suda, J.J. Delaunay, Appl Phys Lett, 95 (2009).

[67] J.F. Li, Y.F. Huang, Y. Ding, Z.L. Yang, S.B. Li, X.S. Zhou, F.R. Fan, W. Zhang, Z.Y. Zhou, Y. WuDe, B. Ren, Z.L. Wang, Z.Q. Tian, Nature, 464 (2010) 392-395.

[68] S.I. Rae, I. Khan, Analyst, 135 (2010) 1365-1369.

[69] Y. Nishijima, Y. Adachi, L. Rosa, S. Juodkazis, Opt Mater Express, 3 (2013).

[70] A. Hartstein, J.R. Kirtley, J.C. Tsang, Phys Rev Lett, 45 (1980) 201-204.

[71] C. Kendall, M. Isabelle, F. Bazant-Hegemark, J. Hutchings, L. Orr, J. Babrah, R. Baker, N. Stone, Analyst, 134 (2009) 1029-1045.

[72] J. Srajer, A. Schwaighofer, G. Ramer, S. Rotter, B. Guenay, A. Kriegner, W. Knoll, B. Lendl, C. Nowak, Nanoscale, 6 (2014) 127-131.

[73] J.M. Hoffmann, H. Janssen, D.N. Chigrin, T. Taubner, Opt Express, 22 (2014) 14425-14432.

[74] L.V. Brown, X. Yang, K. Zhao, B.Y. Zheng, P. Nordlander, N.J. Halas, Nano Lett, 15 (2015) 1272-1280.

[75] R. Adato, H. Altug, Nat Commun, 4 (2013).

[76] C.T. Cooper, M. Rodriguez, S. Blair, J.S. Shumaker-Parry, J Phys Chem C, 119 (2015) 11826-11832.

[77] Y. Nishijima, H. Nigorinuma, L. Rosa, S. Juodkazis, Opt Mater Express, 2 (2012) 1367-1377.

[78] T. Wang, V.H. Nguyen, A. Buchenauer, U. Schnakenberg, T. Taubner, Opt Express, 21 (2013) 9005-9010.

[79] Y.Q. Li, L. Su, C. Shou, C.M. Yu, J.J. Deng, Y. Fang, Sci Rep-Uk, 3 (2013).

[80] A. Hatta, T. Ohshima, W. Suetaka, Appl Phys a-Mater, 29 (1982) 71-75.

[81] M.K. Gunde, M. Kunaver, Appl Spectrosc, 57 (2003) 1266-1272.

[82] Y. Nishikawa, T. Nagasawa, K. Fujiwara, M. Osawa, Vib Spectrosc, 6 (1993) 43-53.

[83] S.Y. Kang, I.C. Jeon, K. Kim, Appl Spectrosc, 52 (1998) 278-283.

[84]http://www.nanotrio.com/board/list.php?category=&board_num=11&rowid=19&go=&sw=&sn=&st=&sc=&page=1.

[85] https://acswebcontent.acs.org/prfar/2013/Paper12279.html.

[86] K. Sumida, D.L. Rogow, J.A. Mason, T.M. McDonald, E.D. Bloch, Z.R. Herm, T.H. Bae, J.R. Long, Chem Rev, 112 (2012) 724-781.

[87] Y.-S. Bae, R.Q. Snurr, Angewandte Chemie International Edition, 50 (2011) 11586-11596.

[88] N.L. Rosi, J. Eckert, M. Eddaoudi, D.T. Vodak, J. Kim, M. O'Keeffe, O.M. Yaghi, Science, 300 (2003) 1127-1129.

[89] M. Dincă, A. Dailly, Y. Liu, C.M. Brown, D.A. Neumann, J.R. Long, J Am Chem Soc, 128 (2006) 16876-16883.

[90] J.R. Li, J. Sculley, H.C. Zhou, Chem Rev, 112 (2012) 869-932.

[91] J.S. Seo, D. Whang, H. Lee, S.I. Jun, J. Oh, Y.J. Jeon, K. Kim, Nature, 404 (2000) 982-986.

[92] S.-C. Xiang, Z. Zhang, C.-G. Zhao, K. Hong, X. Zhao, D.-R. Ding, M.-H. Xie, C.-D. Wu, M.C. Das, R. Gill, K.M. Thomas, B. Chen, Nat Commun, 2 (2011) 204.

[93] J. Lee, O.K. Farha, J. Roberts, K.A. Scheidt, S.T. Nguyen, J.T. Hupp, Chem Soc Rev, 38 (2009) 1450-1459.

[94] D. Dang, P. Wu, C. He, Z. Xie, C. Duan, J Am Chem Soc, 132 (2010) 14321-14323.

[95] T. Uemura, N. Yanai, S. Kitagawa, Chem Soc Rev, 38 (2009) 1228-1236.

[96] M. Albrecht, M. Lutz, A.L. Spek, G. van Koten, Nature, 406 (2000) 970-974.

[97] B. Chen, Y. Yang, F. Zapata, G. Lin, G. Qian, E.B. Lobkovsky, Adv Mater, 19 (2007) 1693-1696.

[98] P. Horcajada, T. Chalati, C. Serre, B. Gillet, C. Sebrie, T. Baati, J.F. Eubank, D. Heurtaux, P. Clayette, C. Kreuz, J.-S. Chang, Y.K. Hwang, V. Marsaud, P.-N. Bories, L. Cynober, S. Gil, G. Ferey, P. Couvreur, R. Gref, Nat Mater, 9 (2010) 172-178.

[99] P. Horcajada, C. Serre, G. Maurin, N.A. Ramsahye, F. Balas, M. Vallet-Regí, M. Sebban, F. Taulelle, G. Férey, J Am Chem Soc, 130 (2008) 6774-6780.

[100] J. Della Rocca, D. Liu, W. Lin, Accounts Chem Res, 44 (2011) 957-968.

[101] L.E. Kreno, K. Leong, O.K. Farha, M. Allendorf, R.P. Van Duyne, J.T. Hupp, Chem Rev, 112 (2012) 1105-1125.

[102] T.-H. Yu, C.-H. Ho, C.-Y. Wu, C.-H. Chien, C.-H. Lin, S. Lee, J Raman Spectrosc, 44 (2013) 1506-1511.

[103] Y. Hu, J. Liao, D. Wang, G. Li, Anal Chem, 86 (2014) 3955-3963.

[104] R.J.T. Houk, B.W. Jacobs, F.E. Gabaly, N.N. Chang, A.A. Talin, D.D. Graham, S.D. House, I.M. Robertson, M.D. Allendorf, Nano Lett, 9 (2009) 3413-3418.

[105] L.E. Kreno, N.G. Greeneltch, O.K. Farha, J.T. Hupp, R.P. Van Duyne, Analyst, 139 (2014) 4073-4080.

[106] L. He, Y. Liu, J. Liu, Y. Xiong, J. Zheng, Y. Liu, Z. Tang, Angewandte Chemie International Edition, 52 (2013) 3741-3745.

[107] L.E. Kreno, J.T. Hupp, R.P. Van Duyne, Anal Chem, 82 (2010) 8042-8046.

[108] A.D. Kersey, T.A. Berkoff, W.W. Morey, Electron Lett, 28 (1992) 236-238.

[109] S.W. James, M.L. Dockney, R.P. Tatam, Electron Lett, 32 (1996) 1133-1134.

[110] H.Y. Choi, K.S. Park, S.J. Park, U.C. Paek, B.H. Lee, E.S. Choi, Opt Lett, 33 (2008) 2455-2457.

[111] H. Berthou, C.K. Jorgensen, Opt Lett, 15 (1990) 1100-1102.

[112] M.G. Xu, L. Reekie, Y.T. Chow, J.P. Dakin, Electron Lett, 29 (1993) 398-399.

[113] H.Y. Fu, H.Y. Tam, L.Y. Shao, X.Y. Dong, P.K.A. Wai, C. Lu, S.K. Khijwania, Appl Optics, 47 (2008) 2835-2839.

[114] Y.N. Ning, Z.P. Wang, A.W. Palmer, K.T.V. Grattan, D.A. Jackson, Rev Sci Instrum, 66 (1995) 3097-3111.

[115] K. Bohnert, P. Gabus, J. Nehring, H. Brandle, J Lightwave Technol, 20 (2002) 267-276.

[116] K. Bohnert, P. Gabus, J. Kostovic, H. Brandle, Opt Laser Eng, 43 (2005) 511-526.

[117] R.C.D.B. Allil, M.M. Werneck, Ieee T Instrum Meas, 60 (2011) 2118-2125.

[118] M.A. Butler, Sensor Actuat B-Chem, 22 (1994) 155-163.

[119] J.M. Fini, Meas Sci Technol, 15 (2004) 1120-1128.

[120] K.M. Leonard, Sensor Actuat B-Chem, 25 (1995) 458-461.

[121] J. Burck, B. Zimmermann, J. Mayer, H.J. Ache, Fresen J Anal Chem, 354 (1996) 284-290.

[122] V. Budinski, D. Donlagic, Sensors-Basel, 17 (2017).

[123] C. Peng, Z.B. Li, A.S. Xu, Appl Optics, 46 (2007) 4125-4131.

[124] W. Jin, Y. Zhou, P.K.C. Chan, H.G. Xu, Sensor Actuat a-Phys, 79 (2000) 36-45.

[125] J. Kalenik, R. Pajak, Sensor Actuat a-Phys, 68 (1998) 350-355.

[126] A. Vallan, M.L. Casalicchio, G. Perrone, Ieee T Instrum Meas, 59 (2010) 1389-1396.

[127] L.Y. Shao, L.Y. Xiong, C.K. Chen, A. Laronche, J. Albert, J Lightwave Technol, 28 (2010) 2681-2687.

[128] Y. Liu, L.L. Zeng, Y.L. Lu, S. Liu, Z.J. Huang, Acta Phys Sin-Ch Ed, 60 (2011).

[129] Y.L. Lo, B.R. Chue, S.H. Xu, Opt Commun, 230 (2004) 287-295.

[130] X.G. Tian, X.M. Tao, Exp Mech, 41 (2001) 248-253.

[131] H. Golnabi, P. Azimi, Opt Commun, 281 (2008) 614-620.

[132] N. Tankovsky, I. Nikolov, K. Baerner, I. Buchvarov, J Opt a-Pure Appl Op, 5 (2003) 1-5.

[133] http://berkshirephotonics.com/products/optical-fiber/.

[134] D. Uttamchandani, Iee P-Optoelectron, 144 (1997) 125-125.

[135] O. Shekhah, H. Wang, S. Kowarik, F. Schreiber, M. Paulus, M. Tolan, C. Sternemann, F. Evers, D. Zacher, R.A. Fischer, C. Woll, J Am Chem Soc, 129 (2007) 15118-+.

[136] A.R. Millward, O.M. Yaghi, J Am Chem Soc, 127 (2005) 17998-17999.

[137] J.M. Schloss, Infrared Spectroscopy of Trapped Gases in Metal-Organic Frameworks, in, Oberlin College Honors Theses, 2011.

[138] F.R. J. Rouquerol, K. S. W. Sing, P. Llewellyn, G. Maurin., Adsorption by Powders and Porous Solids: Principles, Methodology and Applications, Academic Press, 2014.

[139] M. Thommes, K. Kaneko, A.V. Neimark, J.P. Olivier, F. Rodriguez-Reinoso, J. Rouquerol, K.S.W. Sing, Pure Appl Chem, 87 (2015) 1051-1069.

[140] J. Garrido, A. Linaressolano, J.M. Martinmartinez, M. Molinasabio, F. Rodriguezreinoso, R. Torregrosa, Langmuir, 3 (1987) 76-81.

[141] L. Grajciar, A.D. Wiersum, P.L. Llewellyn, J.S. Chang, P. Nachtigall, J Phys Chem C, 115 (2011) 17925-17933.

[142] F. Gul-E-Noor, B. Jee, A. Poppl, M. Hartmann, D. Himsl, M. Bertmer, Phys Chem Chem Phys, 13 (2011) 7783-7788.

[143] J.J. Gutierrez-Sevillano, S. Calero, R. Krishna, J Phys Chem C, 119 (2015) 3658-3666.

[144] G. Korotcenkov, Chemical Sensors: Simulation and Modeling Volume 2: Conductometric-Type Sensors, Momentum Press, 2012.

[145] P. Gandhidasan, A.A. Al-Farayedhi, A.A. Al-Mubarak, Energy, 26 (2001) 855-868.

[146] C. Yildirim, S.K. Soylu, I. Atmaca, I. Solmus, Energ Convers Manage, 85 (2014) 140-145.

[147] K.J. Leckrone, J.M. Hayes, Anal Chem, 69 (1997) 911-918.

[148] J.S. Cha, R. Li, K.K. Sirkar, J Membrane Sci, 119 (1996) 139-153.

[149] S.J. Metz, W.J.C. van de Ven, J. Potreck, M.H.V. Mulder, M. Wessling, J Membrane Sci, 251 (2005) 29-41.

[150] X. Chong, K. Kim, P. Ohodnicki, E. Li, C. Chang, A. Wang, Sensors Journal, IEEE, PP (2015) 1-1.

[151] D. Sonnenfroh, K. Parameswaran, Appl Phys B-Lasers O, 102 (2011) 407-416.

[152] E. Hawe, P. Chambers, C. Fitzpatrick, E. Lewis, Measurement Science & Technology, 18 (2007) 3187-3194.

[153] M.G. Moharam, T.K. Gaylord, J Opt Soc Am, 71 (1981) 811-818.

[154] J.M. Steele, C.E. Moran, A. Lee, C.M. Aguirre, N.J. Halas, Phys Rev B, 68 (2003).

[155] H. Gao, J.M. McMahon, M.H. Lee, J. Henzie, S.K. Gray, G.C. Schatz, T.W. Odom, Opt Express, 17 (2009) 2334-2340.

[156] F.Y. Tian, A.M. Mosier, A. Park, E.R. Webster, A.M. Cerro, R.S. Shine, L. Benz, J Phys Chem C, 119 (2015) 15248-15253.

[157] C.M. Brown, Y. Liu, T. Yildirim, V.K. Peterson, C.J. Kepert, Nanotechnology, 20 (2009) 204025.

[158] J.M. Hoffmann, X.H. Yin, J. Richter, A. Hartung, T.W.W. Mass, T. Taubner, J Phys Chem C, 117 (2013) 11311-11316.

[159] C. Huck, A. Toma, F. Neubrech, M. Chirumamilla, J. Vogt, F. De Angelis, A. Pucci, Acs Photonics, 2 (2015) 497-505.

[160] M. Valamanesh, Y. Borensztein, C. Langlois, E. Lacaze, J Phys Chem C, 115 (2011) 2914-2922.

[161] T.W. Ebbesen, H.J. Lezec, H.F. Ghaemi, T. Thio, P.A. Wolff, Nature, 391 (1998) 667-669.

[162] K.Y. Kim, X.Y. Chong, F.H. Ren, A.X. Wang, Opt Lett, 40 (2015) 5339-5342.

[163] F.H. Ren, K.Y. Kim, X.Y. Chong, A.X. Wang, Opt Express, 23 (2015) 28868-28873.

[164] D. Fairen-Jimenez, S.A. Moggach, M.T. Wharmby, P.A. Wright, S. Parsons, T. Duren, J Am Chem Soc, 133 (2011) 8900-8902.

[165] H.W. Siesler, Near-infrared spectroscopy: principles, instruments, applications, Wiley-VCH, 2002.

[166] M. Lackner, Rev Chem Eng, 23 (2007) 65-147.

[167] N.A. Yebo, W. Bogaerts, Z. Hens, R. Baets, Ieee Photonic Tech L, 23 (2011).

[168] X. Ma, M.Y. Li, J.J. He, Ieee Photonics J, 5 (2013).

[169] B. Momeni, M. Chamanzar, E.S. Hosseini, M. Askari, M. Soltani, A. Adibi, Opt Express, 16 (2008) 14213-14220.

[170] Z.X. Xia, A.A. Eftekhar, M. Soltani, B. Momeni, Q. Li, M. Chamanzar, S. Yegnanarayanan, A. Adibi, Opt Express, 19 (2011) 12356-12364.

[171] S.W. Wang, C.S. Xia, X.S. Chen, W. Lu, M. Li, H.Q. Wang, W.B. Zheng, T. Zhang, Opt Lett, 32 (2007) 632-634.

[172] H.A. Bethe, Physical Review, 66 (1944) 163-182.

[173] C. Genet, T.W. Ebbesen, Nature, 445 (2007) 39-46.

[174] G. D'Aguanno, N. Mattiucci, M.J. Bloemer, D. de Ceglia, M.A. Vincenti, A. Alu, J Opt Soc Am B, 28 (2011) 253-264.

[175] D. de Ceglia, M.A. Vincenti, M. Scalora, N. Akozbek, M.J. Bloemer, Aip Adv, 1 (2011).

[176] Y. Ding, R. Magnusson, Opt Express, 12 (2004) 5661-5674.

[177] K.L. Lee, J.B. Huang, J.W. Chang, S.H. Wu, P.K. Wei, Sci Rep-Uk, 5 (2015).

[178] H. Lochbihler, R.A. Depine, Appl Optics, 51 (2012) 1729-1741.

[179] F.F. Liu, X.P. Zhang, Biosens Bioelectron, 68 (2015) 719-725.

[180] D.B. Mazulquim, K.J. Lee, J.W. Yoon, L.V. Muniz, B.H. Borges, L.G. Neto, R. Magnusson, Opt Express, 22 (2014) 30843-30851.

[181] A.T.M.A. Rahman, P. Majewski, K. Vasilev, Opt Lett, 37 (2012) 1742-1744.

[182] F.H. Ren, K.Y. Kim, X.Y. Chong, A.X. Wang, Opt Express, 23 (2015).

[183] J.D. Driskell, K.M. Kwarta, R.J. Lipert, M.D. Porter, J.D. Neill, J.F. Ridpath, Anal Chem, 77 (2005) 6147-6154.

[184] J. Yang, L. Zhen, F. Ren, J. Campbell, G.L. Rorrer, A.X. Wang, J Biophotonics, 8 (2015) 659-667.

[185] M.E. Webber, R. Claps, F.V. Englich, F.K. Tittel, J.B. Jeffries, R.K. Hanson, Appl Optics, 40 (2001) 4395-4403.

[186] M.E. Webber, S. Kim, S.T. Sanders, D.S. Baer, R.K. Hanson, Y. Ikeda, Appl Optics, 40 (2001) 821-828.